



저작자표시-비영리-변경금지 2.0 대한민국

이용자는 아래의 조건을 따르는 경우에 한하여 자유롭게

- 이 저작물을 복제, 배포, 전송, 전시, 공연 및 방송할 수 있습니다.

다음과 같은 조건을 따라야 합니다:



저작자표시. 귀하는 원저작자를 표시하여야 합니다.



비영리. 귀하는 이 저작물을 영리 목적으로 이용할 수 없습니다.



변경금지. 귀하는 이 저작물을 개작, 변형 또는 가공할 수 없습니다.

- 귀하는, 이 저작물의 재이용이나 배포의 경우, 이 저작물에 적용된 이용허락조건을 명확하게 나타내어야 합니다.
- 저작권자로부터 별도의 허가를 받으면 이러한 조건들은 적용되지 않습니다.

저작권법에 따른 이용자의 권리는 위의 내용에 의하여 영향을 받지 않습니다.

이것은 [이용허락규약\(Legal Code\)](#)을 이해하기 쉽게 요약한 것입니다.

[Disclaimer](#)

Master of Science

**The effects of anode additives towards suppressing
dendrite growth and hydrogen evolution reaction in
metal-air (M=Zn, Fe) secondary batteries**

The Graduate School of the University of Ulsan

Department of Chemistry

Emmanuel Olugbemisola Aremu

**The effects of anode additives towards suppressing
dendrite growth and hydrogen evolution reaction in
metal-air (M=Zn, Fe) secondary batteries**

Supervisor: Professor Kwang-Sun Ryu

A Dissertation

Submitted to

In partial fulfillment of the requirements
for the Degree of
Master of Science

by

Emmanuel Olugbemisola Aremu

Department of Chemistry
The Graduate School of the University of Ulsan
Ulsan, Korea

December, 2019

**The effects of anode additives towards suppressing
dendrite growth and hydrogen evolution reaction in
metal-air (M=Zn, Fe) secondary batteries**

This certifies that the dissertation of Emmanuel Olugbemisola Aremu is approved.

Committee Chair Prof. LEE, Youngil

Committee Member Prof. OH, Eun-Suok

Committee Member Prof. RYU, Kwang-Sun

Department of Chemistry
The Graduate School of the University of Ulsan
Ulsan, Korea

December, 2019

Dedicated to

My Family

And

Loved ones

Abstract

Chapter 1 focuses on the developing a cost effective Zn-air battery and the effects of different anode additives towards suppressing dendrite growth and hydrogen evolution reaction in Zn-air secondary batteries. We revealed interesting findings during an extensive study on Zn-air batteries using 3 wt. % BiO as anode additive. In our continual effort to develop a cost effective rechargeable Zn-air batteries, herewith we demonstrated Zn anodes comprising of (i) 30 wt. % Zn : 3 wt. % bismuth oxide : 10 wt. % potassium sulfide (ZBK) (ii) 30 wt. % Zn : 3 wt. % bismuth oxide : 5 wt. % lead (II) oxide (ZBP) and (iii) 30 wt. % Zn : 3 wt. % bismuth oxide : 10 wt. % potassium sulfide : 5 wt. % lead (II) oxide additives (ZBKP) in 6 M KOH aqueous solutions and 1.88 wt. % polyacrylic acid as the gelling agent. KOH gel constituted the remaining mass of the anode wt. %. Results were confirmed via cycle voltammetry (CV), Tafel, electrochemical impedance spectroscopy (EIS) etc. measurements. Among the various Zn anodes analyzed, ZBKP showed a superior cathodic peak of -1.805 and 1.950 V vs. Hg/HgCl at 5th and 40th cycles during electrochemical cycle voltammetry. Tafel fitting on linear polarization test shows that ZBK exhibits the highest corrosion behavior follow by ZBP while ZBKP has the lowest corrosion behavior with an estimated corrosion inhibition efficiency of 36.06 %. Furthermore, ZBKP display the lowest dendrite growth, least corrosion rate and superior capacity even at 60th cycles compared to ZBK and ZBP. In view of our finding, ZBKP has a higher positive electrode potential compare to ZBK and ZBP electrodes. Thus, ZBKP is the most suitable for aqueous battery due to its low minimal side effect. Field emission-scanning electron microscopy/energy dispersive X-ray spectroscopy (FE-SEM/EDS) images confirm that the various elemental additives were evenly deposited on the Zn anode surface. Ex situ spectroscopy and electrochemical performance studies also verified that the dendrite-free nature of improved Zn anode and the modified interfaces between electrolyte and Zn plays vital roles towards advancing the energy storage performance.

In chapter 2, we report the performance and degradation behavior of carbonyl Fe – MoS₂ composite as anode material in Fe-air batteries using half-cell. We identified hydrogen evolution reaction (HER) and passivation as the two technical limitations of Fe-air batteries. HER account for low charging efficiency while passivation in Fe-air batteries account for its inability to fully discharge at a high rate due to the formation of iron hydroxide. As a result of this, many studies has been dedicated to inhibit these problems. Just like in recent literatures,

the enhancement of Fe-air anode for commercialization is not trivial. With high purity carbonyl Fe-MoS₂ composites electrode and the influence of 2 mM Na₂S additives in 6M KOH electrolyte solution and 1.88 wt. % polyacrylic acid as the gelling agent, we have demonstrated a high performance carbonyl Fe anodes comprising of 3 wt. % MoS₂ (F3M), 5 wt. % MoS₂ (F5M), and 10 wt. % MoS₂ (F10M) additives in Fe anodes. The result of the various electrodes characterized via field emission scanning electron microscopy (FE-SEM) and X-ray diffraction (XRD) reveals a distinct surface morphology that correspond to fundamental crystallographic growth patterns. Additionally, Energy dispersive spectroscopy (EDS) and SEM mapping affirms that both the Fe and additive (weight (wt. %) and atomic percent (at. %)) were well dispersed in the electrode. According to Tafel test, F3M, F5M, and F10M exhibit corrosion inhibition efficiency of 51.2 %, 21.1 % and 5.6 % respectively. Thus, the corrosion rate decreased in the order of bare Fe > F10M > F5M > F3M. While drastic capacity retention drops occur in the bare Fe electrode around 300th cycle, we were able to regenerate the battery back to full capacity via our choice of additives (F3M). During regeneration at 800th cycles, the capacity retention of F3M, F5M, and F10M electrodes were 97%, 93%, and 76%, respectively. Therefore, in conjunction with the unique structure and synergistic effect that characterizes two excellent anode materials, F3M is best choice for a high-performance Fe-air battery due to its excellent performance, low side effects (corrosion and passivation), low float current, superior capacity retention and efficiency during cycling compare to F5M and F10M.

Table of Contents

	Page
Abstract	i
Table of Contents	iii
List of Figures	iv
Lists of Tables	vi
Lists of Equations	vii
Chapter 1. The effects of anode additives towards suppressing dendrite growth and hydrogen gas evolution reaction in secondary Zn-air batteries	
1.1 Introduction	1
1.2 Experimental	5
1.3 Results and discussion	8
1.4 Conclusion	21
1.5 References	
Chapter 2. Performance and degradation behavior of carbonyl Fe – MoS₂ composite as anode material in Fe-air batteries	
2.1 Introduction	27
2.2 Experimental	
2.2.1 Chemicals	29
2.2.2 Material preparation and characterization	30
2.3 Results and discussion	
2.3.1 Characterization and Morphological Study of Fe electrodes	31
2.3.2 Cycle voltammetry (CV) analysis of Fe electrodes	35
2.3.3 Cathodic activation of Fe electrodes	38
2.3.4 Tafel polarization analysis of Fe electrodes	39
2.3.5 Linear polarization resistance analysis of Fe electrodes	41
2.3.6 Capacity retention/efficiency study	42
2.3.7 Energy dispersive X-ray spectroscopy of F3M battery	44
2.4 Conclusions	46
2.5 References	47

List of Figures

	Page
Chapter 1.	
Figure 1.1 Material preparation and three electrodes electrochemical test configuration setup.	6
Figure 1.2 Cathode preparation for full cell test.	7
Figure 1.3 SEM images of (a) unmilled K ₂ S pellet and (b) dried milled K ₂ S powder gotten after 2h of milling process.	8
Figure 1.4 EDS analysis of dried milled K ₂ S powder gotten after 2 h of milling process.	10
Figure 1.5 Powder X-ray diffraction pattern of ZBKP.	11
Figure 1.6 Cycle voltammetry analysis of (a) ZBKP, (b) ZBP, and (c) ZBK electrodes after 40 th cycles at 1 mV/s scan rate.	12
Figure 1.7 Linear polarization of the various Zn anodes at 2.0 V vs. Hg/HgCl.	13
Figure 1.8 Tafel polarization of (a) ZBK, (b) ZBP, and (c) ZBKP electrodes.	15
Figure 1.9 EIS conducted at 0 V (vs. OCV) with AC amplitude of 5 mV and frequency range of 1Hz ~100Hz: (a) Nyquist Plot and (b) Bode plot of $\log Z $ vs. $\log (f)$.	16
Figure 1.10 Cycling data of (a) ZBK, (b) ZBP, and (c) ZBPK electrodes at 50 mAcm ⁻² .	17
Figure 1.11 (a) Specific charge and (b) specific discharge capacities as a function of cycle number at 50 mAcm ⁻² .	18
Figure 1.12 FE-SEM (a & b) and EDS (c & d) analysis of ZBPK before cycling.	19

Chapter 2.

Figure 2.1	XRD pattern for Fe-MoS ₂ composite.	33
Figure 2.2	Fe-SEM images of (a) pure carbonyl Fe, (b) F3M, (c) F5M, (d) F10M and composite (e-g) SEM mapping of Fe and additive distribution in the compound at 20,000x magnification.	34
Figure 2.3	Cyclic voltammograms of various anodes in 6 M KOH electrolyte solutions at a scan rate of 0.17 mV s ⁻¹ over a potential range of -1.4 V to - 0.3 V (vs. Hg/HgCl).	35
Figure 2.4	Cyclic voltammograms of (a) F3M, (b) F5M, and (c) F10M composites in 6 M KOH solution with 2 mM Na ₂ S electrolyte additive over potential range of -1.4 V to - 0.3 V (vs. Hg / HgCl) at a scan rate of 10 mV s ⁻¹ .	37
Figure 2.5	Performance behavior of F10M anode (a-b) in 6 M KOH and (c-d) 6 M KOH + Na ₂ S electrolyte solution upon cathodic activation after anodic and cathodic polarization.	38
Figure 2.6	Tafel plots of (a) bare, (b) F3M, (c) F5M, and(d) F10M	40
Figure 2.7	Current as a function of time of various anodes in (a) 6 M KOH and (b) 6 M KOH solution with Na ₂ S electrolyte additive.	41
Figure 2.8	Batteries cyclability of various electrodes in 6 M KOH + 2 mM Na ₂ S electrolytes.	43
Figure 2.9	Float current of Fe Batteries with different compositions of MoS ₂ Additives.	44
Figure 2.10	EDS images of (a) bare Fe, (b) F3M, (c) F5M, and (d) F10M composites after cycling.	45

List of Tables

	Page
Chapter 1.	
Table 1.1 Merits of BiO, K ₂ S, and PbO additives on several applications (MABs, LIBs, and supercapacitors).	4
Table 1.2 Chemical composition of Zn gel anode samples in 6 M KOH solution.	5
Table 1.3 Variation in chemical composition of dried milled potassium sulfide particles at different time interval.	9
Table 1.4 Cathodic peaks of various Zn anodes employed during CV analysis.	12
Table 1.5 Electrochemical kinetics parameters of Tafel curves.	14
Table 1.6 Weight and atomic percentages of ZBPK anode before and after cycling.	20
Chapter 2.	
Table 2.1 Roles of materials tested in this work.	31
Table 2.2 Anodes behavior in 6 M KOH solution.	36
Table 2.3 Behavior of various anodes in 6 M KOH with 2 mM Na ₂ S electrolyte additive.	38
Table 2.4 Electrochemical kinetics parameters of Tafel curves.	40
Table 2.5 Relative abundance of individual chemical element content present in the electrodes.	45

List of Equations

	Page
Chapter-1	
Equation 1.1 Corrosion inhibition efficiency in Zinc electrode.	13
Chapter-2	
Equation 2.1 Mechanism for reversibility behavior of Fe – Step 1.	28
Equation 2.2 Mechanism for reversibility behavior of Fe – Step 2 .	28
Equation 2.3 Mechanism for hydrogen gas evolution reaction of Fe anode.	28
Equation 2.4 Mechanism for reversibility behavior of MoS ₂ anode.	37
Equation 2.5 Corrosion inhibition efficiency in Fe-MoS ₂ electrode .	39

Chapter 1

The effects of anode additives towards suppressing dendrite growth and hydrogen gas evolution reaction in secondary Zn-air batteries

1.1. Introduction

In recent times, metal air battery has shown significant high energy densities, voltage and capacities. This system is considerably cheap and comes with several other advantages due to the fact that oxygen is the positive electrode reactant. In addition, Zn metal is suitable in aqueous environment and this permits its suitability in aqueous based electrolytes which are cheap and safer to use than non-aqueous based electrolytes. Several metals such as lithium, calcium, aluminum, magnesium, zinc, and iron have been reported, among which, lithium is known to have possess the highest theoretical energy density and an operating voltage of 3.4 V [1-5]. However, the metallic form of Li is unstable in aqueous electrolyte and oxygen. In the case of Al and Mg-air batteries, considerable energy densities like the Li-air have proven to be suitable in aqueous electrolyte. Meanwhile, both Al and Mg air batteries are characterized with low reduction potentials, which account for their sharp self-discharge rate and low columbic efficiency during charging process.

In conjunction with several other literatures, our previous studies highlighted that Fe and Zn shows stability and reversibility in aqueous based electrolyte. In addition, the abundance of these metals, cost effectiveness, environmental benign cannot be over emphasized. While both Fe and Zn based batteries present compelling merits for large scale energy storage, Zn have received more attention because of its higher cell voltage (1.65 V) and energy densities (1300 Wh/g) compare to Fe. However, the commercialization of Zn-air batteries is limited due to catalyzing reaction at the air electrode, ZnO formation, internal resistances and passivation, corrosion of system due to hydrogen gas evolution reaction (HER) and dendrite growth during high charging rate, etc. which limit performance of the cell drastically. As a result, strategies to limit the above drawbacks cannot be step-sided.

Recently, we demonstrated a controlled Zn anode dendrite formation during charging process by high current densities of 0.1 and 0.2 Acm⁻² using bismuth oxide as anode additive. The level of performance achieved in our electrode shows an enhanced improvement. Alternative measures as to enhancing cell performances using electrode and electrolyte additive such as bismuth, cadmium, tin, lead (II) oxide, metal sulfides etc. have been reported but seems to provide insufficient information on how dendrite and HER were partially or completely inhibited, the performance of the electrode during and after inhibition of this harmful effect, the behavior of the electrode upon degradation etc. [6-9].

Notwithstanding, in this current study, we demonstrate more insight into the role of

the K_2S and PbO additives in mitigating dendrite formation and HER in bismuth oxide-Zn air batteries we previously studied. We also report the performance and behavior of the cells upon degradation and the measures taken to improve the cell's performances. During full cell analysis, we prepared air electrode comprising of gas diffusion and reaction layers. Material characterization techniques such as X-ray diffraction pattern (XRD), scanning electron microscopy (SEM) and energy dispersive spectroscopy (EDS) were adopted to extract the phases, morphology and quantities of elemental additives present in the Zn anode. In addition, EIS and Tafel test for bare Zn and ZB anodes were not included in our previous study. However, in this present study, we report the performance of the electrode during EIS and Tafel test analysis for the bare Zn and ZB anodes [8].

Table 1.1 depicts some of the roles of our choice of additives towards improving the performances of electrodes in several applications including supercapacitors, metal-air batteries (MABs) and LIBs have been reported by several researchers. Hence, Zn anode coated with bismuth oxide, potassium sulfide, and lead oxide additives is suitable for complete mitigation of HER and elimination of dendrite growth for enhanced rechargeable Zn-air batteries.

Table 1.1. Merits of BiO, K₂S, and PbO additives on several applications (MABs, LIBs, and supercapacitors).

Additives	Merits	References
Bismuth oxide	<p>MABs: Essential for controlling dendrite formation or short cycle, inhibit HER, alloy workability, improve reversibility, excellent specific capacity etc.</p> <p>Supercapacitors: Good electrochemical performances, high thermal stability (550 ~ 650 °C), good electrical conductivity etc.</p> <p>LIBs: Good cycling, excellent specific capacities, enhance, better efficiency etc.</p>	[8, 22, 25]
Lead(II)oxide	<p>MABs: Good corrosion resistance, high temperature range (260~340°C), high cell potential, long cycle good reversibility.</p> <p>Supercapacitors: Enhanced efficiency, improved cell voltage, good capacity retention, high cycles, high specific energy and power.</p> <p>LIBs: Mechanical stability and durability, alloy workability.</p>	[9-21]
Potassium sulfide	<p>MABs: offers structure effects by altering the alloys microstructure, better cycling, and good cell capacity etc.</p> <p>Supercapacitors: high specific capacitance, extended life cycles (> 5000 cycling).</p> <p>LIBs: improves voltage and overall performances of the cell.</p>	[22-24].

1.2. Experimental

The materials used were Zn metal powder (1 ~ 50 μm), lead (II) oxide (99.99 % purity), potassium hydroxide (93 % purity), potassium hydroxide (93% purity), bismuth oxide, (99.99% purity), and potassium sulfide (99.9 % purity), purchased from Daejung Chemicals, South Korea. Lead (II) oxide (99.5 % purity) was purchased from Junsei chemicals, Japan. Also, polyacrylic acid, 2-propanol, polytetrafluoroethylene (60 wt. % in D.I H₂O), Ni-mesh (99.5 % purity), platinum wire (VS20), and Hg/HgCl reference electrode were purchased from Sigma Aldrich, South Korea.

In our previous study, we prepared Zn metal powder with and without bismuth oxide additives [8]. In this study, our Zn anodes consist of Zn metal powder with BiO, PbO, and K₂S additives. In a separate experiment, we prepared anodes comprising of Zn metal powder + bismuth oxide + PbO (ZBP), Zn metal powder + bismuth oxide + K₂S (ZBK), and Zn metal powder + bismuth oxide + K₂S + PbO (ZBPK) as illustrated in Table 1.2, KOH gel constituted the remaining mass of the anode wt. %. First, the metal powder was prepared by homogenously mixing Zn powder with additives and 15 wt.% PTFE in 2-propanol. The homogenously mixed powders were deposited on a pure Ni-mesh (1 cm \times 2 cm) and subjected to mechanical roll pressing. The total weight of the electrode was 4.25 g and average thickness was ~ 320 μm .

Table 1.2. Chemical composition of Zn gel anode samples in 6 M KOH solution.

Sample	Zn wt. %	BiO wt. %	PbO wt. %	K ₂ S wt. %	PAA wt. %
ZBK	30	3	-	10	1.88
ZBP	30	3	5	-	1.88
ZBPK	30	3	5	10	1.88

*PAA= Polyacrylic acid; KOH gel constituted the remaining mass of the anode wt. %

XRD of the electrode materials was conducted via Rigaku Ultima IV (D/MAX 2500 V/PC, Rigaku, Japan) using Cu radiation ($\lambda = 1.5406 \text{ \AA}$) with a step size of $0.02^\circ/2\theta$ A over the range of $0 \sim 90^\circ$, to confirm the phases of the samples before and after several cyclings. In addition, FE-SEM (JSM-6500F, JEOL, Japan) integrated with EDS was carried out at an accelerating potential of 10 kV on a plot of energy (keV) vs. X-ray counts to study the morphology and elemental information of each elements present in the electrode. Each energy peaks corresponds to the individual elements present in the sample.

During half-cell study, three electrode electrochemical cell configuration was used for all electrodeposition experiments. Nickel foil ($1 \text{ cm} \times 2 \text{ cm}$) composing of Zn-BiO with and without additives (K_2S and PbO) was exposed to 6M KOH electrolyte and used as our working electrode while Hg/HgCl electrode and platinum (Pt) wire were adopted as our reference and counter electrodes respectively as illustrated in Figure 1.1. Cyclic voltammetry (CV) analysis test was carried out at a scan rate of 1 mV/s over a potential range of $-2.0 \sim 0.5 \text{ V}$ vs. Hg/HgCl using IVIUM stat (Ivium technologies, Netherlands). Electrochemical impedance spectroscopy (EIS) was carried out using a potentiostat/galvanostat with impedance measurement unit (SP-300). The EIS measurement was performed at room temperature ($23 \pm 1 \text{ }^\circ\text{C}$) with alternate current (AC) amplitude of 5 mV and frequency range from $1 \text{ Hz} \sim 100 \text{ kHz}$.

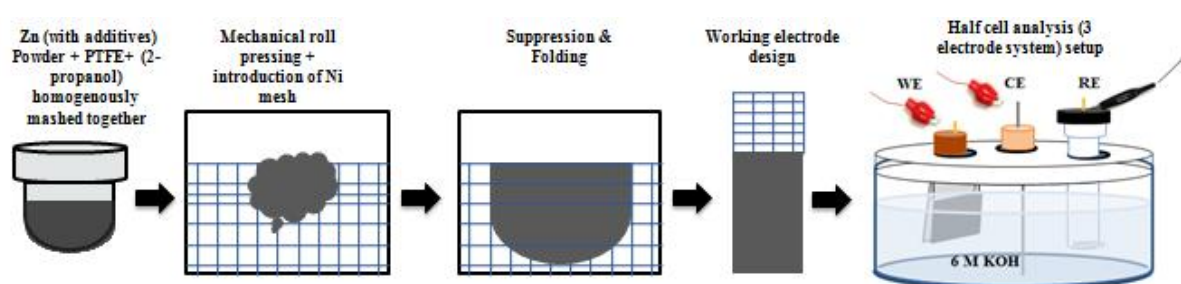


Figure 1.1. Material preparation and three electrodes electrochemical test configuration setup.

* WE = working electrode, CE = counter electrode; RE = reference electrode

During full cell analysis, Zn gel anode was made by mixing 6 M KOH electrolyte solutions with 1.88 wt. % polyacrylic acid as the gelling agent for 2 hours. Thereafter, 30 wt. % Zn powder and additives powders were added at varied wt. % and agitated at 1000 rpm for 10 minutes at room temperature. The homogeneous mixture was employed as our zinc anode while liquid porous film was used as our separator as illustrated in Figure 1.2 below. Galvanostatic cycling test was conducted over a current density of 50 mAcm^{-2} for 120 minutes to monitor the electrode performances during charge and discharge process. Nanostructure potassium sulfide composite size was reduced by grinding under dried condition via SPEX SamplePrep 8000M Mixer/Mill. During the milling process, 4 g of potassium sulfide pellet (average size of 800 nm, purity of 95%) and 50 g of tungsten carbide mill balls ($\text{Ø} = 5 \text{ mm}$) were dispensed inside the milling jar under nitrogen atmosphere using globe box and vacuum packing so as to avoid reaction between oxygen available in the atmosphere and the sulfide particles. Potassium sulfide was acquired by controlling the operating time from 1 to 2 h.

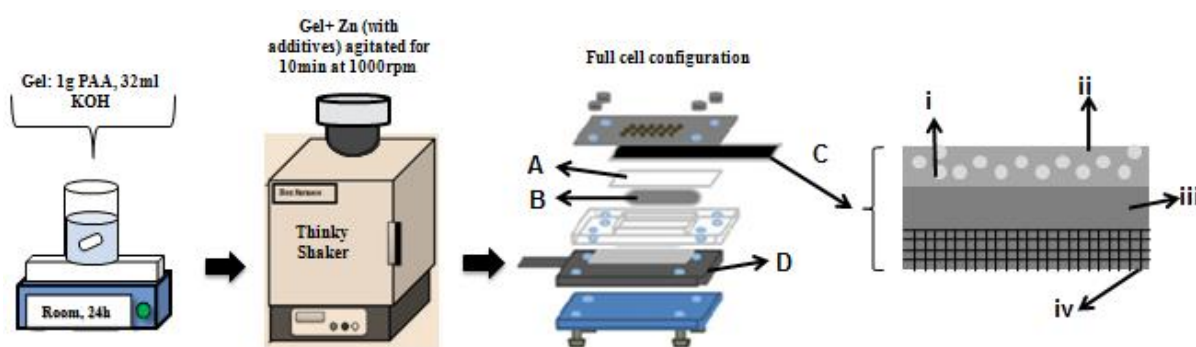


Figure 1.2. Cathode preparation for full cell test (A=Separator; B= anode (Gel + Zn with additives); C= air cathode; D= charge collector; Ci=catalyst; Cii= reaction site; Ciii= carbon cloth; Civ=gas diffusion layer)

1.3. Results and Discussion

The surface morphological structure of the unmilled and dry milled potassium sulfide particles gotten after 1 ~ 2 h is shown in Figure 1.3 (a-b). SEM images of the dried milled K_2S particles shows a well clustered and rough surface morphological structure. In Figure 3b, some of the small bright spots detected by SEM were the tungsten carbide ball particles gotten from the milling jar during the dried milling process. In order to ascertain the atomic and weight percent of the individual element present in the milled particles, we conducted EDS analysis as shown in Figure 1.4. According to EDS, the tungsten carbide balls from the milling jar contaminated the K_2S particles due to the direct collision between the milling balls and the surface of the jar during the milling process. However, in respect to Table 1.3, it should be noted that contamination increases with the milling operating time.

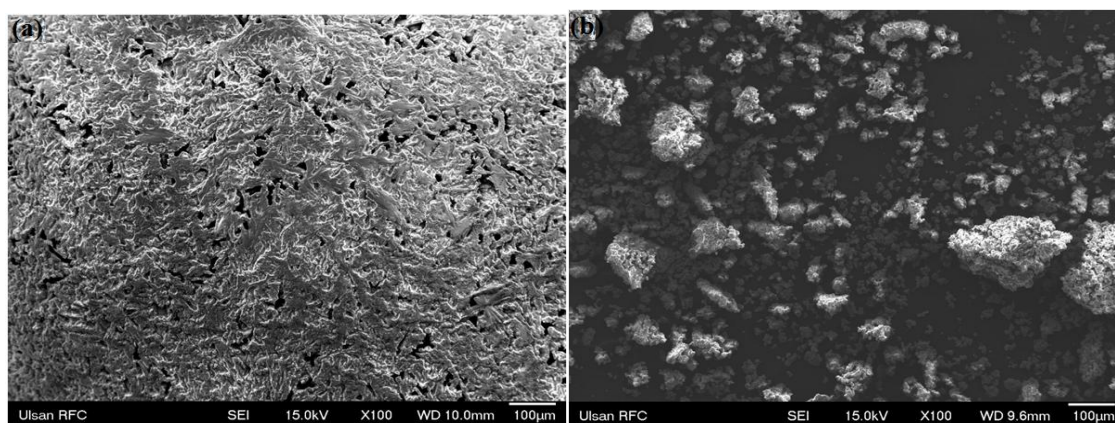


Figure 1.3. SEM images of (a) unmilled K_2S pellet and (b) dried milled K_2S powder gotten after 2 h of milling process.

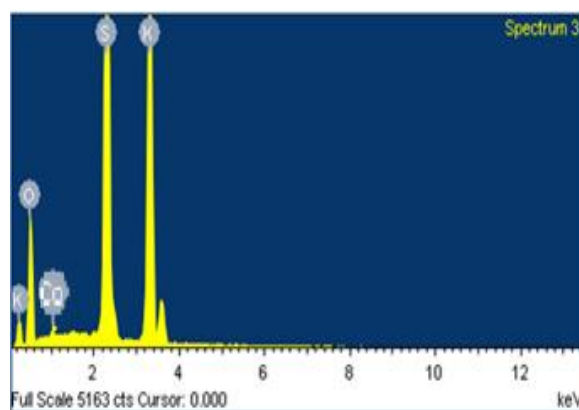


Figure 1.4. EDS analysis of dried milled K_2S powder gotten after 2 h of milling process.

Table 1.3. Variation in chemical composition of dried milled potassium sulfide particles at different time interval.

Element	Un-milled		1 h.		2 h.	
	wt. %	at. %	wt. %	at. %	wt. %	at. %
K	60.41	53.53	57.98	49.38	55.68	46.40
S	36.18	39.09	35.18	36.52	33.72	32.90
O	3.41	7.38	6.75	14.05	10.90	20.00
Co	0	0	0.09	0.05	0.15	0.70
Total	100	100	100	100	100	100

The various phases present in the samples were studied via X-ray powder diffraction (XRD) pattern. The XRD pattern of Zn:BiO:PbO:K₂S composite is shown in Figure 1.5. According to XRD result, the Zn:BiO:PbO:K₂S crystals reflect in various orientations. We observed that the Zn peaks occurred at different intensities, implying different direction of crystal growth (each additives produces a distinct crystalline surface structure). Among the various diffraction peaks observed were the presence of Zn (★), lead (II) oxide (◆), bismuth oxide (■), and potassium sulfide (▲) along 26.65° ~ 86.23° 2-theta axis respectively. Other than this peaks was the presence of Zn oxide (●) situated around 70.03° ~ 77.84°. All diffraction peaks were matched with JCPDS card No. 00-004-0831 (Zn), 00-038-1477 (PbO), 00-014-0699 (BiO), 00-3030-0944 (K₂S), and 01-071-3830 (ZnO), respectively. The narrow, sharp and symmetrical diffraction peaks shows a well crystallized sample with a stable and low baseline. The highest peak had a height (cps) of 55044 (958) around 42.28°. The highest peak is also seen in the XRD pattern of a typical commercial zinc metal. It is worthy to note that the variation in the preferential growth imply that the additives successfully modify the electroplated zinc anode.

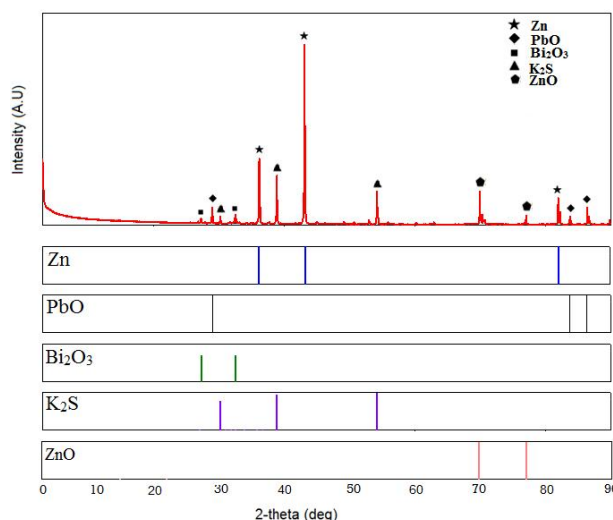


Figure 1.5. Powder X-ray diffraction pattern of ZBKP.

In our previous study, we illustrated the CV for bare Zn and bare Zn : 3wt. % bismuth oxide (ZB) anode [8]. In this present study, we shows CV analysis of ZBK, ZBP, and ZBKP in 6M KOH solution between potential range of -2.0 V vs. Hg/HgCl to -0.5 V vs. Hg/HgCl at a scan rate of 1 mV/s Figure 1.6 (a-c). In order to understand the role of the various additives on the zinc anode's surface, CV measurement was conducted for 40 cycles. Throughout the scanning process, our test analysis displays a single couple redox peak for all the three anodes (ZBK, ZBP and ZBKP). The various samples could sustain redox peaks up to 30th cycles. However, at 40th cycle, no cathodic peak was noticeable in ZBP and ZBK anodes during scanning thereby making it impossible for further reversible reaction to occur. Surprisingly, ZBKP electrode showed cathodic peak of -1.950 V vs. Hg/HgCl at 40th cycle. The fact that reduction peaks was observed at 30th cycle shows that all the Zn anodes were well covered by the various additives employed. This explained to us that a certain quantity of the coated additives is essential for the enhancement of performance in the anode. In this case, cyclability was improved by reduced Zn as in the case of the Zn anodes coated with our choice of additives (BiO, PbO, and K₂S - ZBKP). The 1st, 5th, 15th, 20th, 30th, and 40th reduction peaks of the individual Zn anodes coated with additives are illustrated in Table 1.4.

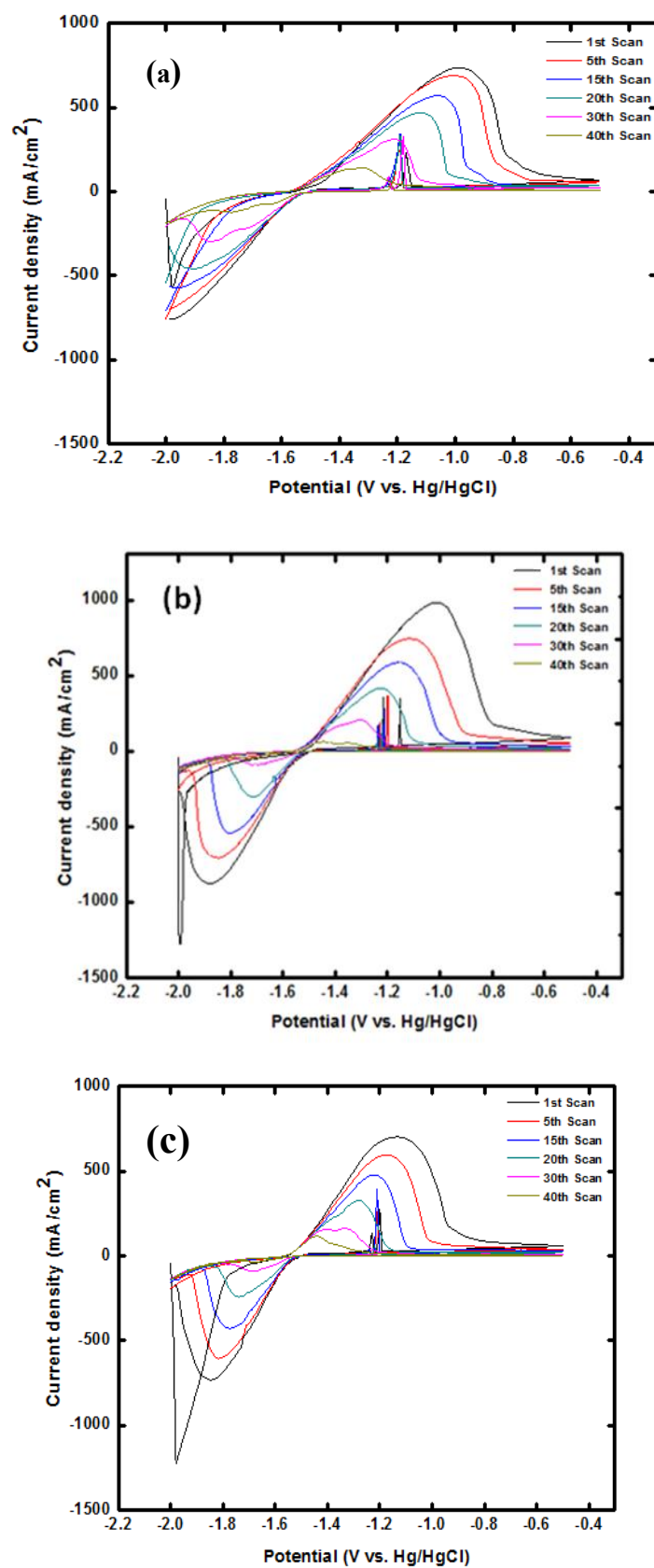


Figure 1.6. Cycle voltammetry analysis of (a) ZBKP, (b) ZBP, and (c) ZBK electrodes after 40th cycles at 1 mV/s scan rate.

Table 1.4. Cathodic peaks of various Zn anodes employed during CV analysis.

Samples	Cathodic peaks (V vs. Hg/HgCl)					
	1 st	5 th	15 th	20 th	30 th	40 th
ZBK	-1.880	-1.850	-1.780	-1.625	-1.638	-
ZBP	-1.800	-1.789	-1.738	-1.655	-1.619	-
ZBPK	-1.950	-1.905	-1.880	-1.845	-1.805	-1.756

The plot of current density as a function of time conducted at 2.0 V vs. Hg/HgCl for 2000 seconds for ZBK, ZBP, and ZBKP anodes is shown in Figure 1.7. In order to avoid duplication of report, refer to our previous study for information about the linear polarization behavior of bare zinc and ZB anodes [8]. In this case, superior rise in current was clearly observed in the ZBKP compare to ZBK and ZBP respectively. Generally, polarization resistance is favored by high current density. The sudden increase in current in ZBKP implied a larger polarization resistance compare to ZBK and ZBP. In addition to our findings, the response-time plot was more flattened and constant current was best maintained in ZBKP anode.

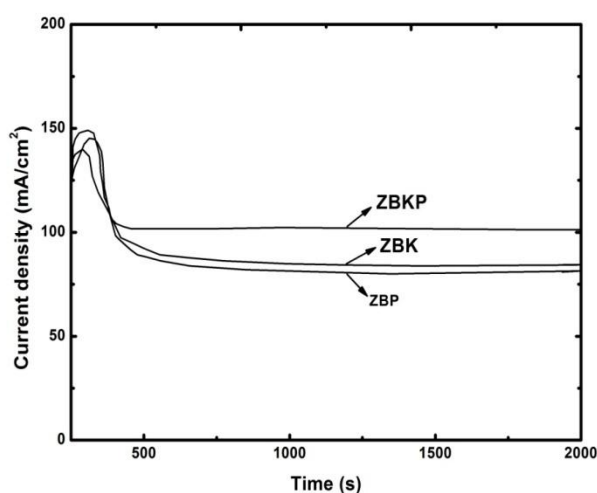


Figure 1.7. Linear polarization of the various Zn anodes at 2.0 V vs. Hg/HgCl.

To understand the effects of our anode additives on the corrosion and polarization behavior of the Zn anode, we conducted Tafel test as shown in Figure 1.8 below. Table 1.5 shows the electrochemical kinetics parameter as well as the current density (j_{corr}), corrosion potential (E_{corr}), and efficiency of inhibition ($E.I\%$) gotten from Tafel test. Both E_{corr} and j_{corr} were estimated from the fitting linear equations of current density as a function of potential while the efficiency of inhibition was estimated using the formula in equation 1.1 below [25, 29]:

$$E. I \% = (j_{\text{corr}}^0 - j_{\text{corr}}) / (j_{\text{corr}}^0 \times 100) \quad [1.1]$$

From equation (1.1) above, j_{corr}^0 and j_{corr} represent the current density when corrosion was taking place at the various electrodes (ZBK, ZBP, and ZBPK). Ostensibly, E_{corr} of ZBPK is positively shifted at varying proportion compared to ZBK and ZBP electrodes. The E_{corr} of ZBK, ZBP, and ZBPK occurred at -1.37 V vs. Hg/HgCl, -1.36 V vs. Hg/HgCl, -1.34 V vs. Hg/HgCl. Likewise, j_{corr} of ZBPK are lower than ZBK and ZBP respectively. This implied that ZBPK exhibited the lowest current density and thus highest corrosion inhibition efficiency. Hence, ZBPK has a more positive electrode potential compare to ZBK and ZBP electrodes, respectively.

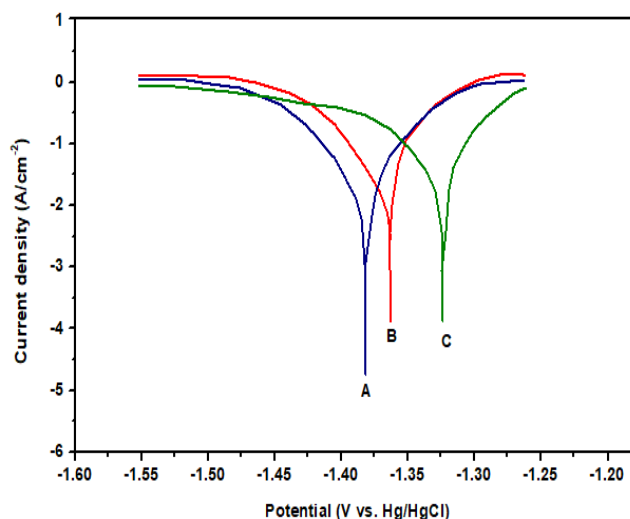


Figure 1.8. Tafel polarization of (a) ZBK, (b) ZBP, and (c) ZBPK electrodes.

Table 1.5. Electrochemical kinetics parameters of Tafel curves.

Samples	j_{corr} (mA cm ⁻²)	E_{corr} (Vvs. Hg/HgCl)	E.I %
ZBK	2.0×10^{-2}	-1.3823	-
ZBP	1.62×10^{-2}	-1.3624	19.0
ZBPK	1.47×10^{-2}	-1.3235	36.06

Electrochemical impedance spectroscopy (EIS) measurements are carried out to investigate the role (behavior and charge transport kinetics) of various anode additives on the impedance via AC amplitude of 5.0mV and frequency range of 1Hz ~ 100 kHz. Figure 1.9 (a-b) depicts the Nyquist plot and Bode plot of impedance spectra of ZBK, ZBP, and ZBKP anodes. All Nyquist plots comprises of a low frequency (LF) straight line and a semicircular loop of high frequency (HF) capacitive. The double layer capacitance parallel to the charge transfer resistance (CTR) accounts for the semicircular loop of HF capacitive, while the gradient of the LF region is due to the diffusion of electrolyte solution in the zinc electrode [30]. The equivalent circuit adopted to fit the EIS is also shown in Figure 1.9a, where R_{ct} designates the CTR and R_s designates total ohmic resistance (resistance of the electrode materials, current collector, and electrolyte). LF straight line is known to reveal the diffusion process of electrolyte in the zinc anode equivalent to constant phase angle element 1 (CPE1) while the constant phase angle element comprising of the layer capacitance designates (CPE2). Based on the equivalent circuit, the fitted R_s of the bare Zn, ZBK, ZBP and ZBKP anodes were 1.0185 Ω , 0.5483 Ω , 0.4495 Ω , and 0.3614 Ω respectively. It is worthy to note that a smaller the R_s will yield a superior electrical conduction. Thus, a superior conductive network was established within the whole active materials of ZBKP due to the decrease in R_s . Likewise, the fitted R_{ct} of the bare Zn, ZBK and ZBP anodes are 4.6858 Ω , 2.9863 Ω , and 2.1507 Ω respectively while that of ZBKP anode is 1.5020 Ω . Generally speaking, a larger R_{ct} displays a complex electrochemical reaction which will consequently result to a high electrochemical polarization. Meanwhile, our analyses clearly reveal how ZBKP anode displays the least R_{ct} among others which imply that ZBKP could be more suitable to lower the impedance during the reaction process.

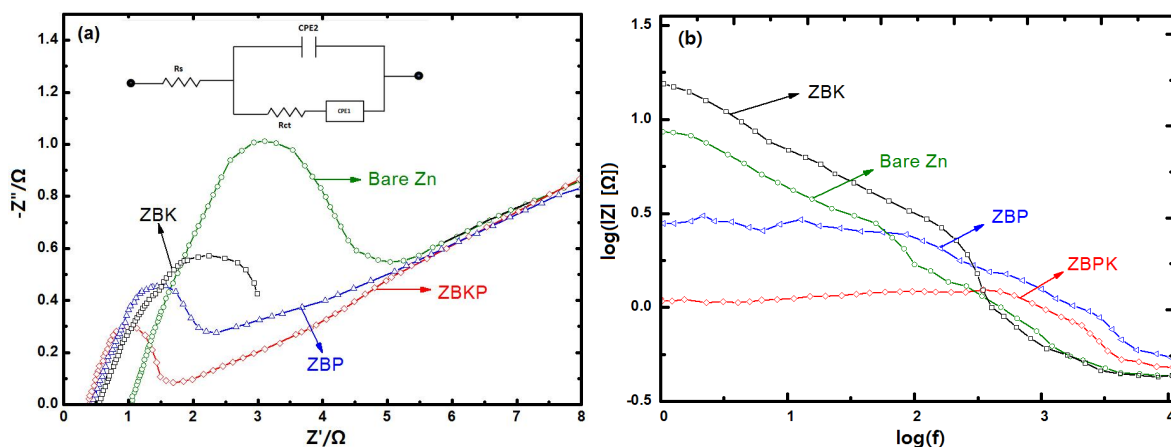


Figure 1.9. EIS conducted at 0 V (vs. OCV) with AC amplitude of 5 mV and frequency range of 1Hz ~100Hz: (a) Nyquist Plot and (b) Bode plot of $\log |Z|$ vs. $\log(f)$.

As shown in Figure 1.9a, the imperfect semi-circle of ZBK in Nyquist plot was as a result of the breakdown and formation of passivation films that keeps occurring at the surface of the anode. By introducing PbO to the anode's surface, the diameter of the semi-circular capacitance loop increased further. In addition, Bode plots of $\log |Z|$ as a function of $\log(f)$ was conducted to study the impedance variation as a function of frequency as depicted in Figure 1.9b. In the case of Bode plot, LF region designates the CTR (R_{ct}) [31]. Bare Zn anode exhibited the least CTR showing a charge transfer kinetic reactions that has to do with the redox process. ZBP and ZBKP revealed higher CTR implying that the anode's surface was occupied by our various elemental additives. We observed that ZBK displayed highest resistance due to formation of passive layer at the surface of the anode. Thus, our result suggested that ZBP and ZBKP exhibited lower impedance compared to ZBP. Also, our result was consistent with the result of potentiodynamic polarization and CV analysis.

For Zn air batteries, we investigated reversibility by using air catalyst as cathode while ZBK, ZBP, and ZBKP were adopted as anode. In Figure 1.10 (a-c), the Zn electrodes were galvanostatically charged and discharged for a period of 2-h at 50 mAcm^{-2} current densities, the cell discharge voltage ranges from 1.0 ~ 1.2 V vs. Hg/HgCl for the various electrodes. No noticeable voltage drop was observed due to the stability the Zn electrodes. In ZBK and ZBP electrodes, continuous discharge occurs until when the Zn metal was completely exhausted in the electrode. From our previous study, ZB could sustain 20 cycles. However, in this present study, we discover that replacing the consumed ZB by simple

combination of PbO and K₂S as in ZBPK electrode gave rise to a regenerated battery that could survive several cycles in Figure 1.10(a-c). The number of cycles sustained by the various electrodes were 40 (ZBK), 50 (ZBP), and 60 (ZBKP), respectively at 100% depth of discharge.

Figure 1.11 (a-b) shows the specific capacity as a function of cycle number. During discharge, we found out that the capacity of ZBP was lower in the first cycle due to partial activation of active materials. Upon further cycling, active material is more and more activated completely. And as a result of this, there was a gradual increase in capacity for ZBP electrode in the initial C/10. The initial formation capacity of the ZBP electrode was (C/1) of 120 mAh/g-Zn and 375 mAh/g-Zn respectively during discharge and charging process. As it can be grasp, the discharge capacity of the ZBP electrode started decreasing after C/10 and was able to maintain a steady charge capacity of 130 mAh/g-Zn at around C/30 ~ C/40 before capacity faded out. Such loss was due to the formation of ZnO, an electrically insulating layer noticed during discharge process which gave rise to passivation [28, 29, 32]. In the case of ZBK electrode, the initial capacity of ZBK was around 100 mAh/g-Zn and 280 mAh/g-Zn during charge and discharge process respectively. Upon further cycling at C/10, capacity decreases to 145 mAh/g during charging process before it eventually remained stable (C/20 ~ C/30) at 125 mAh/g-Zn prior to capacity fade out (C/40). Such drop may be due to the formation of extended dendrite on the surface of the anode. The high surface area of ZBK possibly increases the chance of the dendrite and leads to the failure of the battery. When dendrites grow, the surface of zinc anode increased, and thus the corrosion effect will be more severe. This may explain the good battery performance of ZBKP anode due to absent of dendrite formation and low corrosion currents [30, 31]. Despite the fact that no dendrite was formed in ZBP, passivation occurred. A longer life cycle with superior capacity was obtained through the addition of PbO additives to the ZBK anode which gave rise to the ZBPK. Surprisingly, the ZBPK electrode showed a longer life cycle (C/60) compare to the previously analyzed electrodes as well as higher initial specific capacity (C/1) of 150 mAh/g-Zn and 400 mAh/g-Zn during discharge and charging process. During charging process, the electrode was able to maintain a long stable capacity of 115 mAh/g-Zn at C40 ~ C/60 before capacity faded out.

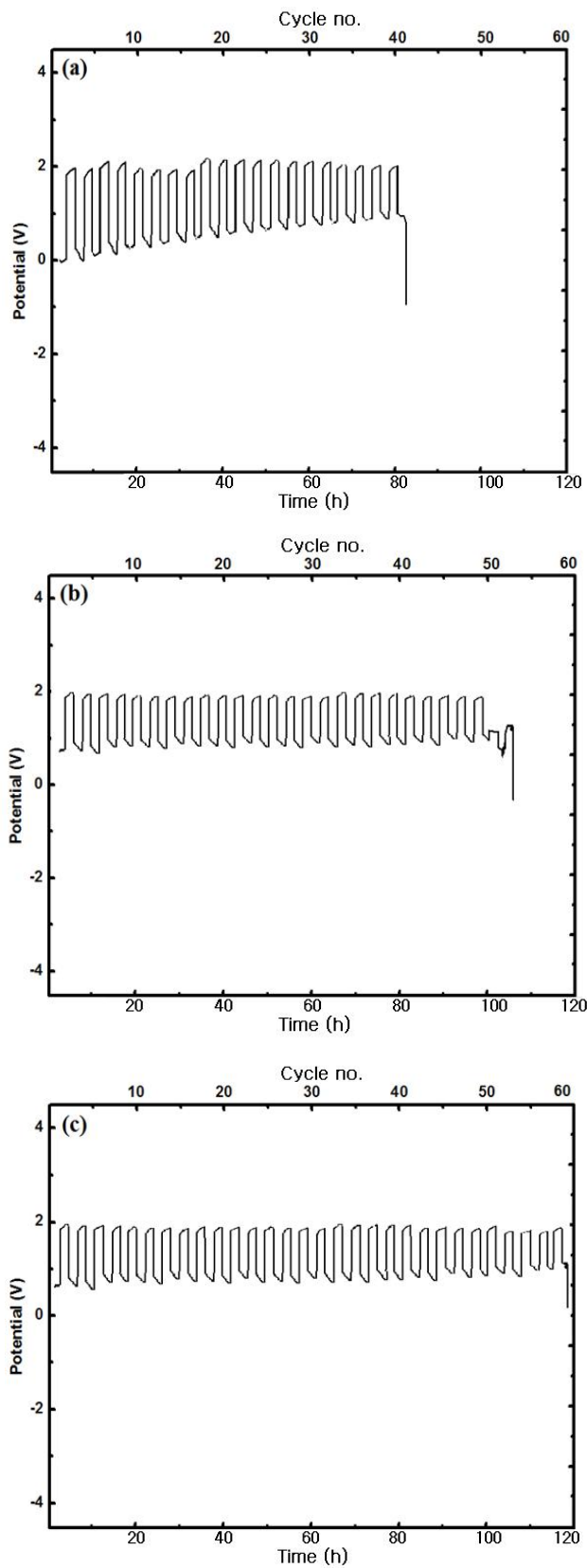


Figure 1.10. Cycling data of (a) ZBK (b) ZBP, and (c) ZBPK electrodes at 50 mAcm^{-2} .

In addition to our findings, no dendrite or passivation was formed in ZBKP electrode. Thus, the presence of bismuth additive mitigates dendrite formation. While sulfides forms a conductive pathways to inhibit passivation of the electrode during discharge. Moreover, there need to further elucidate on the mechanism of de-passivation. Likewise, the presence of PbO additive inhibits hydrogen gas evolution and further suppresses the formation of ZnO to extend the cell's cycle life of cells [33, 34]. Among the various anodes, ZBKP is the most preferred because it was able to solve the problems associated with commercialized zinc anode by improved the capacity of the battery and reduces the side reactions (dendrite formation and corrosion).

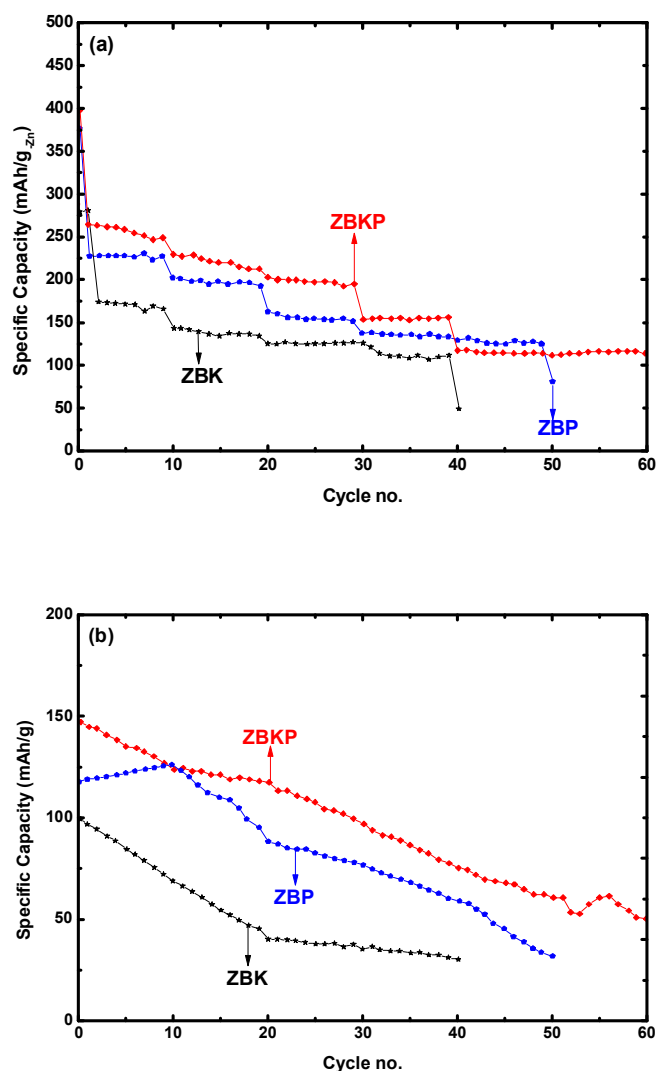


Figure 1.11. (a) Specific charge and (b) specific discharge capacities as a function of cycle number at 50 mAcm⁻².

The morphology of the ZBKP is shown in Figure 1.12 (a-b). The SEM image shows a smooth hexa-lamella with needle like surface structure. This imply that an exact proportion of the elemental additives do not alter the lattice structure of the active materials. The atomic % and weight % of the elemental additives present in the various electrodes before and after cycling confirmed via EDS analysis (Figure c-d) is shown in Table 1.6. In addition to the various elemental additives presents in the anode, we observed that one of the peaks below 3eV corresponds to oxygen which was present in the electrode. The amount of oxygen found was 6.55 wt. % and 5.42 wt. % before and after cycling respectively. It is clear enough that the percentage of our elemental additives (Bio, PbO, and K₂S) deposited on the Zn electrodes before and after cycling was slightly more than what we expected. In addition, EDS could not detect the Co impurity that was present in the drilled milled K₂S as earlier detected. This could be due to imprecision made by our EDS analyzer but nevertheless, the various additives remained in the Zn anode after cycling.

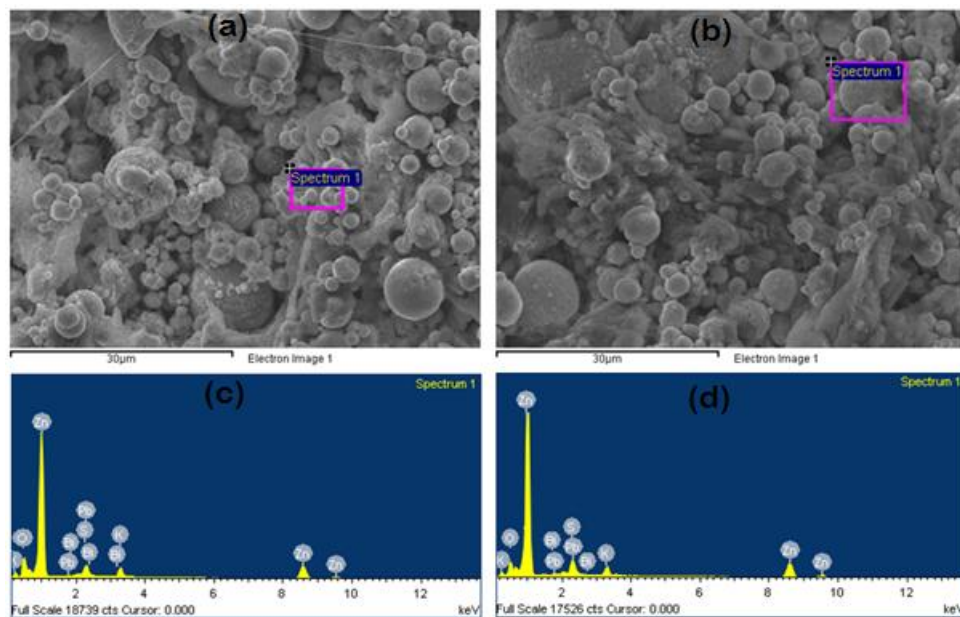


Figure 1.12. FE-SEM (a & b) and EDS (c & d) analysis of ZBKP before cycling.

Table 1.6. Weight and atomic percentages of ZBPK anode before and after cycling

Samples	Before		After	
	wt. %	at. %	wt. %	at. %
Zn	70.85	60.02	71.33	62.43
Pb	5.18	1.38	5.21	1.44
O	6.55	22.52	5.42	19.27
K	10.0	7.05	10.18	7.42
S	4.78	8.26	4.85	8.62
Bi	2.94	0.77	3.01	0.82
Total	100	100	100	100

1. 4. Conclusion

Our past study shows ZB anode with traces of dendrite formation around the Zn anode. CV test analysis revealed an excellent performance ZB anode that could maintain 20 cycles during scanning process. In our continual effort to develop a high performance and cost effective rechargeable Zn air batteries, we investigated ZBK, ZBP, and ZBPK electrodes respectively in 6 M KOH solution. Results were confirmed via CV, EIS, and impedance etc. measurements. During CV analysis, the ZBK and ZBP exhibited noticeable cathodic peak up till 30th cycle. For the first time, we have shown that ZBPK anode had superior electrochemical performance with cathodic peak -1.805 and 1.950 V vs. Hg/HgCl at 5th and 40th cycle at a potential range of -2.0 ~ 0.5 V vs. Hg/HgCl and scan rate of 1 mV/s. During cycling study, the number of cycles sustained by the various electrodes were 40 (ZBK), and 50 (ZBP) and 60 (ZBKP), respectively at 100% depth of discharge before capacity loss. By the combination of additives to the surface of the Zn anode, capacity was regenerated. Concurrently, gradual capacity loss persists even upon the addition of additives. We have ascertained that the capacity fade out in Zn electrode was as a result of dendrite growth on the surface of the Zn electrode during discharge. Tafel polarization test revealed that ZBK has the highest corrosion behavior followed by ZBP while ZBKP has the lowest corrosion behavior with an estimated corrosion inhibition efficiency of 36.06 %. Thus, it is worth noting that ZBKP anode shows superior electrochemical performance when compared to ZBK and ZBP electrode in terms of cell capacity and impedance. Ex situ spectroscopy and electrochemical performance studies also verified that the dendrite-free nature of improved Zn anode and the modified interfaces between electrolyte and Zn plays vital roles towards advancing the energy storage performance. Hence, the level of improvement we demonstrated in this current study is attractive for the design of an advanced secondary zinc-air batteries.

1.5. References

1. S.K. Kamali, V.V. Tyagi, N.A. Rahim, N.L. Panwar, H. Mokhlis, Emergence of energy storage technologies as the solution for reliable operation of smart power systems: A review, *Renewable and Sustainable Energy Reviews*, 25 (2013) 135–165.
2. O.G.P. Jorge, J.R.R. Anthony, P.V. Sofia, L.M. Vitor, M. Jordan, B. Alistair, F.G. Carol, A.W. David, J.H. Peter, Aqueous batteries as grid scale energy storage solutions. *Renewable and Sustainable Energy Reviews*, 68 (2017) 1174–1182.
3. K.S. Prakash, P. Balasundar, S. Nagaraja, P.M. Gopal, V. Kavimani, Mechanical and wear behaviour of Mg–SiC–Gr hybrid composites, *Journal of magnesium and alloys*, 4 (2016) 197–206.
4. J. Fu, Z.P. Cano, M.G. Park, A. Yu, M. Fowler, Z. Chen, Electrically rechargeable zinc-air batteries: progress, challenges, and perspectives. *Advanced materials*, 29 (2017) 1604685–1604685.
5. J. Winsberg, T. Janoschka, S. Morgenstern, T. Hagemann, S. Muench, G. Hauffman, J.F. Gohy, M.D. Hager, U.S. Schubert, Poly(TEMPO)/Zinc hybrid-flow battery: A Novel, “Green,” high voltage, and safe energy storage system, *Advanced Materials*, 28 (2016) 2238–2243.
6. J. Fu, J. Zhang, X. Song, H. Zarrin, X. Tian, J. Qiao, L. Rasen, K. Li, Z. Chen, A flexible solid-state electrolyte for wide-scale integration of rechargeable zinc–air batteries, *Energy and Environment Science*, 9 (2016) 663–664.
7. B. Hwanga, E. Ohb, K. Kim, Observation of electrochemical reactions at Zn electrodes in Zn-air secondary batteries, *Electrochimica Acta*, 216 (2016) 484–489.
8. D.J. Park, E.O. Aremu, K.S. Ryu, Bismuth oxide as an excellent anode additive for inhibiting dendrite formation in zinc-air secondary batteries, *Applied Surface Science*, 456 (2018) 507–514.
9. J. Zhang, R. Xu, B. Yu, Y. He, Y. Li, Z. Qin, Study on the properties of Pb–Co₃O₄–PbO₂ composite inert anodes prepared by vacuum hot pressing technique, *Royal Society of*

- Chemistry Advances, 7 (2017) 49166–49168.
10. X.C. Zhong, X.Y. Yu, L.X. Jiang, F. Li, J. Li, Y.X. Li, Electrochemical behavior of Pb–Ag–Nd alloy during pulse current polarization in KOH solution, *Hydrometallurgy*, 131 (2013) 144–157.
 11. P. Qinmin, W. Zijia, L. Jia, Y. Geping, G. Min, PbO@C core–shell nanocomposites as an anode material of lithium-ion batteries, *Electrochemistry Communications*, 11 (2009) 917–920.
 12. H. Sivaram, D. Selvakumar, A. Alsalme, A. Alswieleh, R. Jayavel, Enhanced performance of PbO nanoparticles and PbO–CdO and PbO–ZnO nanocomposites for supercapacitor application, *Journal of Alloys and Compounds*, 731 (2018) 55–63.
 13. G.P. Miomir, D. Aleksandar, On the use of platinized and activated titanium anodes in some electrodeposition processes, *J. Solid State Electrochemistry*, 1 (1997) 208–214.
 14. X. Wenjing, H. Shen, Y. Sun, J. Guanglou, H. Bing, W. Jian, Performance of PbO₂ on the basis of porous graphite/Pb conductive substrates for hybrid supercapacitors, *Micro & Nano Letters*, 13 (2018) 122–126.
 15. M. Clancy, C.J. Bettles, A. Stuart, N. Birbilis, The influence of alloying elements on the electrochemistry of lead anodes for electrowinning of metals: A review, *Hydrometallurgy*, 131 (2013) 144–157.
 16. C. Cachet, C. Rerolle, R. Wiart, Kinetics of Pb and Pb–Ag anodes for zinc electrowinning-ii. oxygen evolution at high polarization, *Electrochimica Acta*, 41 (1996) 83–90.
 17. A. Mirza, M. Burr, T. Ellis, D. Evans, D. Kakengela, L. Webb, J. Gagnon, C. Leclercq, A. Johnson, Corrosion of lead anodes in base metals electrowinning, *Journal of Southern African Institutes of Mining And Technology*, 116 (2016) 533–537.
 18. Z. Zhao, Z. Chuncheng, L. Zihui, Y. Ying, Z. Yuxin, S. Yu, All-solid-state Al air batteries with polymer alkaline gel electrolyte, *Journal of Power Sources*, 251 (2014) 470–475.
 19. M. Martos, J. Morales, L. Sanchez, Lead-based systems as suitable anode materials for

- Li-ion batteries, *Electrochimica Acta*, 48 (2003) 615–621.
20. N. Jiangfeng, W. Haibo, Q. Yaohui, G. Lijun, PbO₂ electrodeposited on graphite for hybrid supercapacitor applications., *Physica Scripta*, 87 (2013) 045802–045811.
 21. M. Torabi, S.H Razavi, Electrochemical evaluation of Pbo nanoparticles as anode for Lithium ion batteries, *International Journal of Engineering Transactions B: Applications* 24 (2011) 348–351.
 22. A.K. Manohar, C. Yang, S. Malkhandi, G.K.S. Prakash, S.R. Narayanan, Recent advances in inexpensive aqueous batteries for large scale electrical energy storage, *Journal of the Electrochemical Society*, 160 (2013) A2078–A2084.
 23. Manohar, A.K.; Yang, C.; Narayanan, S.R. The role of sulfide additives in achieving long cycle life rechargeable iron electrodes in alkaline batteries. *Journal of the Electrochemical Society*, 162 (2015) A1864–A1872.
 23. Y. Xingwen, M. Arumugam, A voltage enhanced, low cost aqueous Iron–air battery enabled with a mediator-ion solid electrolyte, *ACS Energy Letters*, 2 (2017) 1050–1055.
 24. O. Jorge, P. Gil, J.H. Peter, The effect of electrolyte additives on the performance of iron based anodes for nife cells, *Journal of the Electrochemical Society*, 162 (2015) A2036–A2043.
 25. W. Tingting, Y. Zhanhong, Y. Bin, W. Ruijuan, H. Jianhang, The electrochemical performances of Zn-Sn-Alhydrotalcites in Zn-Ni secondary cells, *Journal of Power Source*, 257 (2014) 174–180.
 26. X. Yu, A. Manthiram, Long life, high voltage acidic zn–air batteries. *ACS Energy Letters*, 2 (2017) 1050–1055.
 27. D.Q. Zeng, Z.H. Yang, S.W. Wang, Preparation and electrochemical performance of In-doped ZnO as anode material for Ni–Zn secondary cells, *Electrochimica Acta*, 56 (2011) 4075–4080.
 28. D.E. Turney, J.W. Gallaway, G.G. Yadav, R. Ramirez, M. Nyce, S. Banerjee, Y.K. Chen-Wiegart, L. Wang, M.J. D’Ambrose, S. Kolhekar J. Huang, X. Wei, Rechargeable zinc

- alkaline anodes for long cycle energy storage, *Chemistry of Materials*, 29 (2017) 4819–4832.
29. W. Long, Z. Yang, X. Fan, B. Yang, Z. Zhao, J. Jing, The effect of carbon on the electrochemical performances of ZnO in Ni-Zn secondary batteries, *Electrochimica Acta*, 105 (2013) 40–46.
 30. S. Hosseini, L. Woranunt, S.J. Han, A. Arpornwichanop T. Yonezawa, S. Kheawhom, Discharge performance of Zinc-air flow Batteries under the effects of sodium dodecyl sulfate and pluronic F-127, *Scientific Report*, 8 (2018) 14909–14916.
 31. J. Chotipanich, A. Arpornwichanop T. Yonezawa, S. Kheawhom, Electronic and Ionic conductivities enhancement of Zinc Anode for Flexible Printed Zinc-Air Battery. *Engineering Journal*, 22 (2009) 1135–1145.
 32. T.X. Xiao, H. Wen, H.H Bao, Y. Yang, Zhen Y.G, L.W. Xing, Dendrite-free lithium anode enables the lithium/graphite dual on Battery with much improved cyclic stability, *ACS Applied Energy Mater*, 2 (2019) 201–206.
 33. E.K. Kyung, K.A.H. Tuan, The Nam Long Doan, Y. Yu, X. Zhu, Y. Tian, P. Chen, Suppression of dendrite formation and corrosion on zinc anode of secondary aqueous batteries, *ACS Applied Materials Interfaces*, 9 (2017) 9681–9687.
 34. H. Duan, Y.X. Yin, Y. Shi, P.F. Wang, X.D. Zhang, C.P. Yang, J.L. Shi, R. Wen, Y.G. Guo, L.J. Wan, Dendrite-free Li-metal Battery enabled by a thin asymmetric solid electrolyte with engineered layers, *Journal of American Chemical Society*, 140 (2018) 82–85.

Chapter 2

Performance and degradation behavior of carbonyl Fe – MoS₂ composite as anode material in Fe-air batteries

2.1. Introduction

Compare to several other types of metal air batteries, considerable interest has been dedicated to the iron air batteries owing to their undeniable characteristics such as long life, absence of dendrite formation at the anode, and high theoretical capacity [1-2]. However, the two technical limitations of iron-air batteries are (1) Hydrogen evolution reaction (HER) (2) Passivation. HER account for the low charging efficiency of a typical iron electrode. For example, the iron electrodes of a conventional commercial alkaline Ni-iron battery have a charging efficiency of not more than 60%. In order to achieve full capacity, iron electrodes need to undergo an overcharged rate. This low charging efficiency has been a continual issue since the earlier report on Fe electrode and it uses was received. Therefore, an overcharged rate of 100% or total mitigation of HER during charging is crucial for the implementation of commercial scale iron-air batteries [3-4]. Secondly, commercial scale batteries must also be able to fully discharge their capacity within the shortest possible time. For example, some grid scale services require batteries of high discharge rate within a concise time interval [5]. However, in order to achieve a high electrode utilization of ≥ 0.2 Ah/g, a typical commercial Fe electrode takes ≥ 4 h to fully discharge its capacity [6-7]. This discharge process is accompanied by the formation of an insulating layer of iron (II) hydroxide responsible for the cell voltage drop of iron electrodes. Therefore, the inability of iron electrode to fully discharge at a high rate due to the formation of iron hydroxide is known as passivation.

Recently, HER on metals like magnesium, iron, and aluminum has gained significant attention owing to their technological and fundamental relevance [8]. However, more attention is focused on the behavior of the metals in solution during HER while lesser attention is channel on how to depassivate the $\text{Fe}(\text{OH})_2$ at the surface of the electrode during reduction process. As previously reported, the HER occurring in metals is generated during the active corrosion that is associated to the local passivation – that emerges from the formation of a poorly protected film or direct exposure of the metal surface to the solution. During this process, a large potential is initially produced across the affected regions. Next, HER will occur to make the affected region to act as current amplifier. The aftermath is the production of current at a region far away from corrosion site (anodic region) [9-12].

Apart from the HER occurring at the cathodic region during corrosion, there is also an occurrence known as “cathodic activation” which is more evident in metals such as aluminum, iron, magnesium, etc. Cathodic activation occurs when the cathodic activity of uncorroded sites is remarkably less than the cathodic activity of corroded sites. In this case,

the metal surface changes from gray to dark before and after undergoing corrosion. As a result of this, cell degradation progresses at higher rate at the dark surface than on the gray surface [13-16]. Therefore, during cathodic activation process, the increase in HER occurring at the cathodically activated sites is associated with the increase in overall rate of HER at free corrosion potential. This will later lead to a local HER associated to an increased anodic current that is available during corrosion. For clearer comprehension, it is crucial that we remind ourselves of the electrochemical reaction of Fe electrodes during cycling process. For Fe electrode, the discharge process occurs in the following steps as illustrated below:



During discharge process in equation (1), Fe is converted to Fe(OH)₂. The high kinetic redox reaction in equation 2.1 favors the formation of Fe₃O₄ in equation 2.2. It is worthy to note that the major product during discharge process is Fe(OH)₂ while Fe₃O₄ would only occur at high anodic potential. However during the charging process of Fe electrode, Fe(OH)₂ is reduced to Fe in equation 1. Also, H₂O is decomposed to produce H₂ as shown in equation 2.3. When this process occur, the energy that is stored in the cell is dissipated in the HER thereby leading to the rapid reduction of the over performance of the Fe electrode.



However, the roles of impurities in passivation and HER of iron electrodes have been revealed since the earliest reports on Fe–air batteries. Iron metal consists of impurities such as calcium, magnesium, phosphorus, and manganese which favor HER. Based on recent studies, high purity materials like carbonyl Fe have been reported to mitigate HER significantly. Also, several researchers reported that sulfides as electrode additive (such as FeS, Bi, BiS, K₂S, etc.) or electrolyte additive would improve the discharge rate by inhibiting the formation of iron hydroxide insulating materials [17]. However, in this study, MoS₂ is our choice of additive in carbonyl Fe. For Fe-MoS₂ composites, the experimental study is not trivial since it is possible to determine the performance and behavior of the electrode. The advantages of our choice of additive have been documented for different alkaline and metal-air batteries electrodes [18]. Yufei *et al.*, Limin and Shinjun reported a reasonably high charge transfer and sharp discharge rate for Li-ion batteries coated with MoS₂ [19-20]. Tan *et al.*, revealed how the sulfide ions in MoS₂ increased the ionic conductivity of the passive film [21]. Honglin *et al.*, channeled their perspective toward the dynamic electron transfer in connection with conductivity and HER [22]. According to Jue *et al.*, HER in MoS₂ is

kinetically retarded in alkaline solution with a low Tafel slope of 76 mV/dec and very low HER over potential of 76 mV at 10 mAcm⁻² [23]. Bin *et al.* stated that MoS₂ supported the electrode with a long cycle life without decay and high capacity. Also, the electrode with MoS₂ is capable of delivering an initial capacity higher than the theoretical value [24-25]. Yongqiang *et al.*, postulated that doping of metal electrode with MoS₂ would reduce compressive stress, increase conductivity and improved charge and discharge rate capability [26]. Thus, with efficiencies of 96, 35 and 40% for charge, energy and voltage respectively, specific charge capacity of <300 Ahkg⁻¹ and an OCV of 1.28V, the iron/air system could find its operation in a range of technologies, including automotive [27-28].

2.2. Experimental

2.2.1. Chemicals

The materials used were: Carbonyl iron powder ($\geq 99.5\%$), molybdenum (IV) sulfide (90 nm, 99 % purity), sodium sulfide (99.5 % purity), polyacrylic acid, 2-propanol, polytetrafluoroethylene (60 wt.% in D.I H₂O), Ni-mesh (99.5 % purity), platinum wire (VS20), and mercury - mercury chloride (3 M KCl), silver nitrate (99.99 % purity), graphite (USGS24), were purchased from Sigma Aldrich, South Korea. Potassium hydroxide (93 % purity) was purchased from Daejung Chemicals, South Korea. Also, Carbon cloth (ELAT LT1400W) was purchased from FuelCell, USA.

2.2.2. Half-cell material preparation and characterization

2-propanol and polytetrafluoroethylene (PTFE) served as solvent and binder respectively. 15 wt.% PTFE was added to 85 wt.% of carbonyl Fe powder. Among the carbonyl Fe electrodes studied, MoS₂ was added at about 3, 5 and 10 wt.% of the powder mixture. Upon the addition of PTFE to the powder mixture, a dough was formed which was used to fabricate the anodes. The iron anodes were fabricated by depositing the dough (powdered mixture) on a pure Ni-mesh followed by mechanical roll pressing at 475 Kg cm⁻². The pressed electrodes were further sintered under nitrogen atmosphere at 300 °C. About 2.25 g of carbonyl Fe powder was distributed over an area of 16.2 cm² providing an active mass loading of 139 mg cm⁻² in the electrode. Electrodes testing were carried out in a three-electrode cell system. Previous study revealed that Hg/HgCl exhibited a stable potential for our kind of electrolyte [29], so Hg/HgCl (3 M KCl) was used as reference electrode and Pt

mesh (2 cm × 2 cm) as counter electrode. 6 M KOH was used as our aqueous solution. Cycle voltammetry and potentiostatic polarization were carried out via IVIUMSTAT Tech. on a completely charged electrodes over at a scan rate of 0.17 mV s⁻¹ over a potential range -1.4 ~ 0.3 V. On a separate experiment, we carried out the same study using 2 mM Na₂S as additives to the 6 M KOH electrolyte solution at a scan rate of 10 mV s⁻¹ over a potential range -1.4 ~ 0.3 V. X-ray diffraction (XRD) of the electrode material was conducted via Rigaku Ultima IV (Cu K α source) to confirm the crystallographical pattern of the samples. Field emission scanning electron microscopy and Energy dispersive spectroscopy mapping (FE-SEM / EDS, Carl Zeiss Supra 40) analysis were carried out to study the morphological structure and relative abundance of individual elements present in the compound.

2.2.3. Full cell material preparation and characterization (Air cathode & Iron gel anode)

The air cathode (Gas diffusion electrode - GDE) was prepared using catalyst ink (CI) and gas diffusion ink (GDI), graphite (KS44) and carbon cloth. At first, GDI was prepared via ultrasonic dispersion of graphite, dispersing agent and water. Next, PTFE dispersion was introduced into the mixture. In the same way, CI consisted of 10 mg/cm² silver catalyst, dispersion agent, 15 wt. % PTFE, graphite powder and water. The prepared GDI and CI were continuously deposited uniformly on the surface of the carbon cloth until the required amount was achieved. Then the electrode was calcined for 3.5 h at a temperature of 80°C (around 353 K). Our study utilizes oxygen present in the air as cathode, the diffusion layer, current collecting layer, and a catalytic active layer stacked in this order, made-up the air-cathode membrane.

Likewise, the Iron gel anode was made by mixing 60.4 wt. % 6 M KOH electrolyte solutions with 1.88 wt. % Polyacrylic acid as the gelling agent for 24 hours. Thereafter, 37.7 wt. % Fe powder and MoS₂ additive were added at varied wt.% (F3M, F5M, and F10M) and agitated at 1000 rpm for 10 minutes at room temperature. The resulted homogeneous mixture and liquid porous film were used as anode and separator respectively. Galvanostatic cycling test was conducted over a current density of 50 mAcm⁻² for 120 minutes to monitor the electrode performances during charge and discharge process. Table 1. depicts the roles of various materials employed during this study.

Table 2.1. Roles of materials tested in this work.

ID	Materials	Roles
01	Graphite	Increase conductivity and permeability.
02	Current collector	Reduces hydrogen evolution reaction (HER).
03	Saturated calomel electrode (Hg /HgCl) – Reference electrode	Shown to be effective with our choice of electrode.
04	Platinum wire	Permit current migration.
05	KOH and Na ₂ S electrolyte solution	Permits reversibility and stability of our choice of electrodes.
06	Anode + 15 wt.% PTFE binder (60% in D.I H ₂ O).	Improve cycle life at high DoD, high redox peak, and increase wettability.
07	Carbon cloth	Same as ID-01 (supply channel for reaction site).
08	Teflon film (air side)	Permeability.
09	Silver powder (ca. < 1 μm diameter)	As catalyst.
10	Screwed component	Provides adequate pressure and contact for the cell.
11	Wrapped electrode in cellophane	Reduce zinc migration.
12	Separator	Retain zinc anode and permits free migration of electrolytes.
13	Deep cycle test	Deeper depth of cycling.

2.3. Results and Discussion

2.3.1. Characterization and Morphological Study of Fe electrodes

The X-ray diffraction (XRD) results of the Carbonyl Fe with and without the MoS₂ additives are represented in Figure 2.1. According to the XRD results, the Fe crystals grow in several orientations. For the commercial Fe, the highest peak intensity for the XRD pattern is situated at 44.73°. This implies that the Fe growth occurs majorly in (110) orientation. Other notable orientations are (002), (020), (103), (110), (105), (200), and (211). These peaks show

similarity with the literature [6]. The combination of our additives also support the high orientation at (110) peak. Using the intensity of plane (110) as reference, the peak intensities ratio (IR) of the various orientations is normalized. According to Figure 1, the IR between XRD peaks at 44.73° and 65.22° is 4.72. This depicts that Fe (110) peak differs amidst other patterns and Fe is the major constituent of the peaks situated at 44.73° . Due to the different intensities that characterizes a fundamental crystallographic growth peak, the Fe-MoS₂ additive displays a distinct growth along the crystalline surface structure. However, the disparity in the surface structure ascribes to the tendency of MoS₂ additive to transform the surface energy of the composite. Thus, at lower surface energy, the crystal growth is favorable. In addition, the experimental approach may be another reason for the intensity disparity in XRD peaks [31-32]. The transformation in the preferential growth of F3M and F5M crystals from (200) to (110) reveals that both 3 wt. % and 5 wt. % MoS₂ improves the surface structure of the Fe anode thereby leaving the probable crystallographic surface to the Fe metal anode. Also, the preferential Fe growth in (110) reveals the possibility of high current efficiency upon deposition of Fe ions.

Specifically, in the XRD pattern of F3M, the Fe crystal is predominantly produced in (110) even though the preferential intensity of F10M shows similarity with the commercial Fe metal. It is worth noting that F3M appreciably reduced the peak intensity (200) which is the succeeding peak to Fe (110) plane. According to Jorge and Peter, the current efficiency at (110) plane is lower than the current efficiency at (200) plane [2]. Of course we also observed and affirmed this fact at the surface of F3M crystal. As a result of this, the growth at (110) is almost parallel to the surface of the electrode, while (200) favors the growth at 44.73° to the electrode surface. This suggest to us that the orientation along (200) plane is less inert compare to the orientation at (110). Therefore, the probability of HER to occur at the (200) plane is less. To further affirm this fact, F3M displays superior peaks at (002) and (110) which correspond to the fundamental crystal growth pattern. Thus, HER is very unlikely to occur at the surface of the Fe electrode with this composition of our choice of additive [31]. In F10M, the intensities of the peak (002) and (211) reveal low intensities while (103) and (105) peaks were not found. In this case, HER is very likely to occur because the crystal growth is perpendicularly aligned to the sample's surface. The Fe-MoS₂ 5 wt.% has high (200) but does not display (105) planes. Hence, an insignificant HER that is less than that of F10M will occur. According to XRD pattern, the likelihood of HER occur in F10M >> F5M >> F3M crystals.

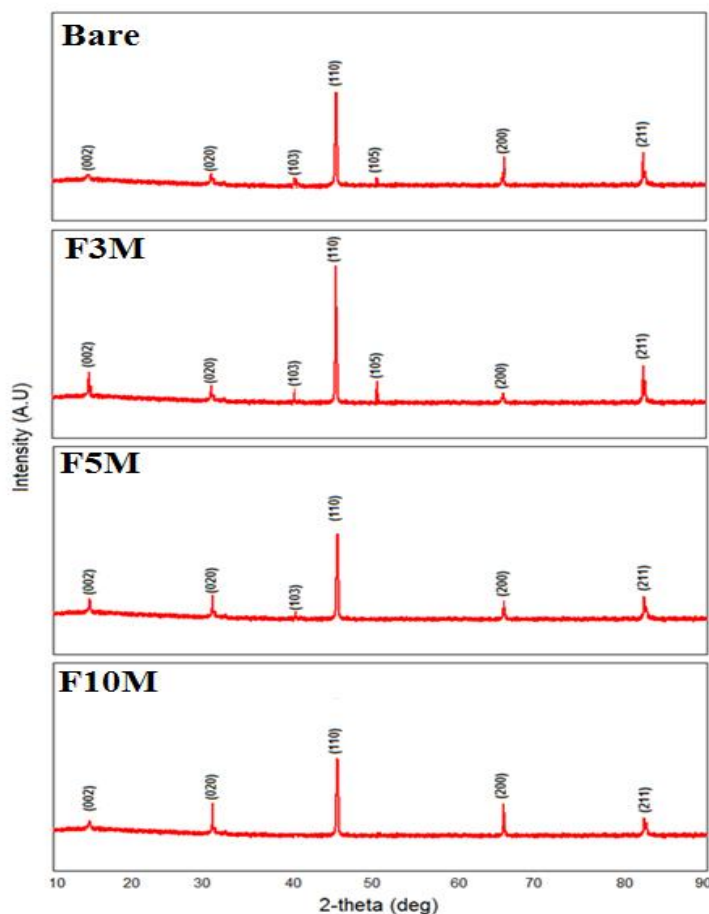


Figure 2.1. XRD pattern for Fe-MoS₂ composite.

The morphology of the Fe electrode in Figure 2.2(a) is uniform and regular but looks slightly scratchy. Figure 2.2(b-d) shows the morphology of the F3M, F5M and F10M respectively. For F3M, SEM image also shows uniform and regularly distributed morphology which depicts that the Fe growth occurs perpendicularly along the various directions of the substrate. This nature of morphology is achievable when the nucleation rate and active sites are reduced during absorption of the 3wt. % MoS₂ additives on the substrate's surface. The F5M surface looks compacted while F10M is less compacted compare to F5M. However, some parts have hollows surface which suggests that HER obstructed the deposition of MoS₂ additive on the surface of the electrode [30]. The SEM mapping in Figure 2.2(e-g) indicated that the Fe and MoS₂ additive were uniformly dispersed in the electrode.

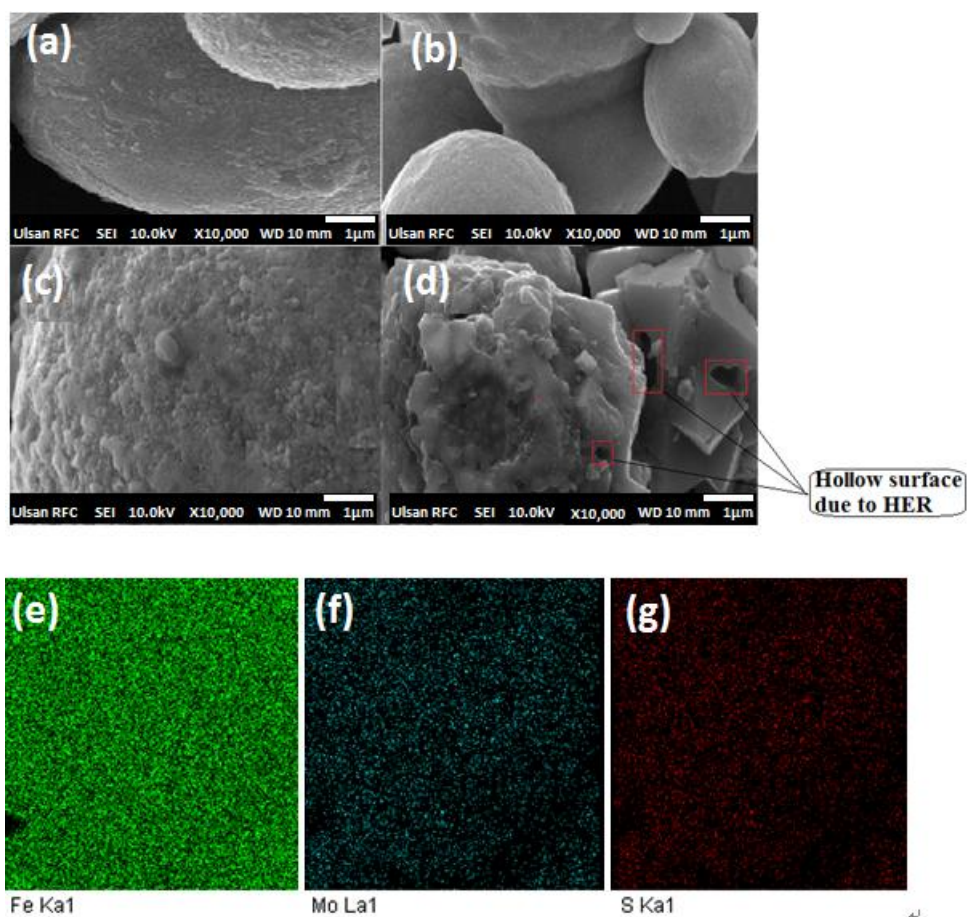


Figure 2.2. Fe-SEM images of (a) pure carbonyl Fe (b) F3M (c) F5M (d) F10M composite, and (e-g) SEM mapping of Fe and additive distribution in the compound at 20,000x magnification.

2.3.2. Cycle voltammetry (CV) analysis of Fe electrodes

Figure 2.3 shows the cycle voltammetry (CV) test conducted at ambient temperature for carbonyl Fe with and without MoS₂ additives at a scan rate of 0.17 mV s⁻¹ over a potential range of -1.4 ~ 0.3 V against 6 M KOH electrolyte solution. During the slow scan rate, several redox peaks that are associated to the reduction of Fe (II)/Fe and Fe (III)/Fe were observed during the cycling process. The observation of several peaks as reported in this present study show similarity with previous literatures. However, the fact that not all past studies reported the presence of the number of peaks we report in this present study is worth noting [1, 5, 33]. These peaks are associated to the presence of Fe at various sites in MoS₂ to form Fe_xMoS₂. Most of the oxidation peaks lie within potential range of -1.17 V to -0.5 V as summarized in Table 2.2. As a result of the reaction taking place between the Fe and MoS₂ phases, four different peaks were observed during the anodic cycling. However, we observed that when potential was applied, there was no concentration gradient around the layers which remained even at several sweeps. Thus, redox process does not occur throughout the surface of the electrode.

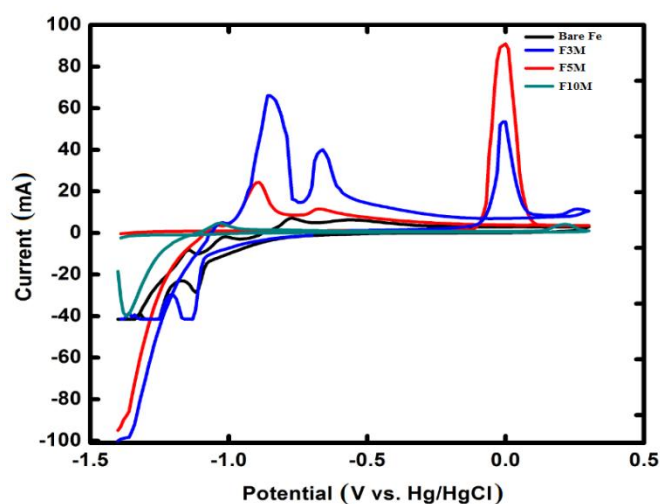


Figure 2.3. Cyclic voltammograms of various anodes in 6 M KOH electrolyte solutions at a scan rate of 0.17 mV s⁻¹ over a potential range of -1.4 V to - 0.3 V (vs. Hg/HgCl).

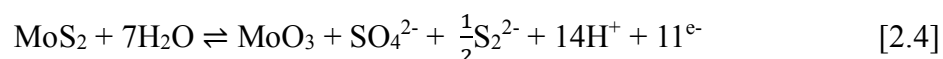
Table 2.2. Anodes behavior in 6 M KOH solution.

Anodic peaks (V vs. Hg / HgCl)						
Sample/peaks	1 st	2 nd	3 rd	4 th	5 th	6 th
Bare Fe	-1.17	-1.03	-0.75	-0.50	-	-
F3M	-1.15	-1.08	-0.98	-0.75	0.14	0.25
F5M	-1.16	-1.05	-0.75	-0.52	-	-
F10M	-1.14	0.26	-	-	-	-
Cathodic peaks (V vs. Hg / HgCl)						
Bare Fe	-1.12	-1.13	-	-	-	-
F3M	-1.05	-1.18	-1.30	-1.35	-	-
F5M	-1.18	-1.30	-1.35	-	-	-
F10M	-1.38	-	-	-	-	-

In comparison with other electrodes, F3M anode shows superior redox peaks in 6 M KOH electrolyte solution. As the potentials of the anodic peaks were shifted to a more positive region the cathodic peaks were shifted to a more negative region as the current decreases. Overall, the number of cathodic peaks observed during reduction was less than the peaks during oxidation. Most of these peaks were evidently observed within a potential range of -1.0 V to -1.38 V. The anodic peak observed at around 0.1 V in F3M and F5M is associated to a thicker formation of Fe (II) and Fe (III) oxide films in KOH electrolyte solution. As current increases, passivation was formed within the electrode while HER was been inhibited [24, 25, 34]. CV test reveals that F5M was not cathodically active in 6 M KOH electrolyte solution. Similar behavior is seen in F10M within a potential range of 0.3 V to -1.18 V in Figure 2.3. Due to the incomplete reduction process, there was an increased over-potential associated to the irreversibility of the reactions, which appears to be the oxidation of Mo^{4+} to Mo^{6+} occurring at the edge and basal regions. However, beyond a potential range of -1.18 V, reduction could occur.

Out of curiosity, special interest was devoted to further study the behavior of the various electrodes with MoS_2 additive in 6 M KOH solution with 2 mM Na_2S as electrolyte additive. Likewise, in order to ensure a stable electrolyte pathway without altering the structure of the electrode, we raised the scan rate from 0.17 mV s^{-1} to 10 mV s^{-1} for 50 cycles. Figure 2.4(a-c) shows the behavior of the electrodes in 6 M KOH with Na_2S electrolyte additive during the

1st, 15th, 30th and 50th scans respectively. It is interesting to note that the electrodes show similar reversibility pattern throughout the scanning process. This suggests that a stable electrolyte pathway was maintained within the electrodes. The lowering of the onset potential of HER is associated with the electron transfer kinetics supporting the electrode [34, 35]. Thus, CV analysis could reveal single redox peak throughout the scanning process as summarized in Table 2.3. Recognition of such peaks like the ones we reported here may be associated to the responsiveness of the electrochemical analysis, reduction of MoO₃ to Mo³⁺ or breaking down of MoO₃ into solution. This is illustrated in equation 2.4 below:



Upon further scanning, similar potential was observed without significant shift towards the positive or negative region. Thus, the reaction maintained a long-range reversibility behavior.

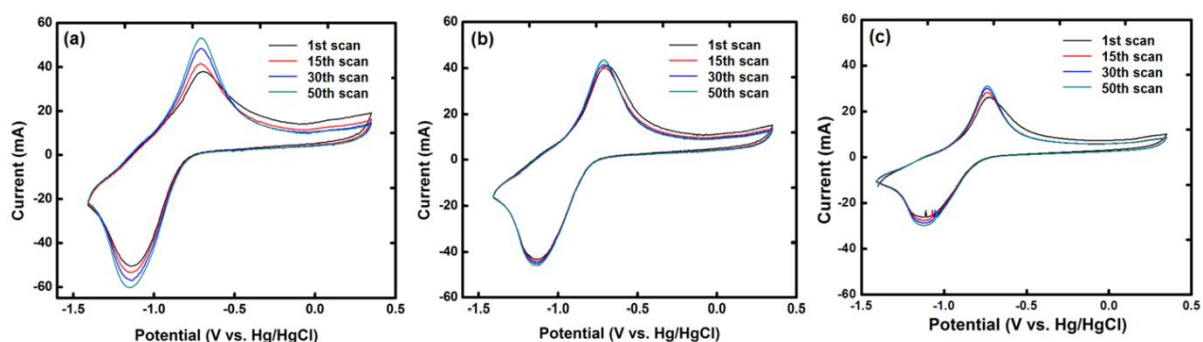


Figure 2.4. (a-c) Cyclic voltammograms of (a) F3M, (b) F5M, and (c) F10M composites in 6 M KOH solution with 2 mM Na₂S electrolyte additive over potential range of -1.4 V to -0.3 V (vs. Hg / HgCl) at a scan rate of 10 mV s⁻¹.

Table 2.3. Behavior of various anodes in 6 M KOH with 2 mM Na₂S electrolyte additive.

Anodic peaks (V vs. Hg/HgCl)				
Sample/cycles	1 st	15 th	30 th	50 th
F3M	-0.58	-0.64	-0.63	-0.63
F5M	-0.63	-0.64	-0.65	-0.64
F10M	-0.63	-0.63	-0.63	-0.63

Cathodic peaks (V vs. Hg/HgCl)				
Sample/cycles	1 st	15 th	30 th	50 th
F3M	-1.20	-1.20	-1.21	-1.23
F5M	-1.00	-1.11	-1.00	-1.05
F10M	-1.12	-1.12	-1.23	-1.23

2.3.3. Cathodic activation of Fe electrodes

Cathodic activation occurs in the F10M electrode. This side reaction was observed after the F10M electrode undergoes passivation at the anodic region due to the relatively high current associated to HER. Among the entire electrolyte solutions that were prepared, cathodic activation was only observable in the 6 M KOH electrolyte containing Na₂S additive. Irrespective of the mechanism that induced the preferential oxidation and the passive film rupture of the electrode, an accumulation of the cathodically active material (MoS₂) during the oxidation process exposed the F10M composites to the formation of stable pits around the surface of the electrode as illustrated in Figure 2.5(a-d).

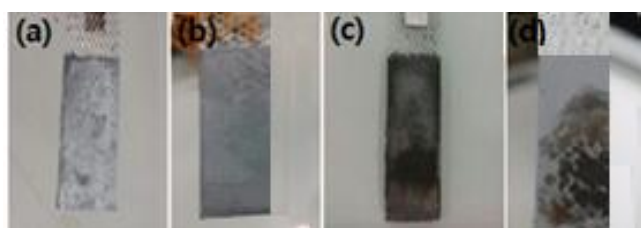
**Figure 2.5.** (a-d) Performance behavior of F10M anode (a-b) in 6 M KOH, and (c-d) 6 M KOH + Na₂S electrolyte solution upon cathodic activation after anodic and cathodic polarization.

Figure 2.5(a-b) shows the state of the F10M electrode in 6M KOH electrolyte solution after anodic and cathodic polarization process took place. In this case, cathodic activation did not occur at the surface of the electrode. However, significant electrode passivation was observed. Out of curiosity to mitigate the passivation effect, we investigate the performance behavior of the F10M anode using 6M KOH with 2mM Na₂S as additive in the electrolyte solution. According to Figure 2.5(c-d), F10M electrode exhibits dark regions around the surface of the electrodes. This dark region represents the cathodic activation site [17]. At cathodic activation region, a relatively high cathodic current is said to be capable of maintaining the corrosion site where HER is taking place. As time progresses, the active corrosion region formed during anodic polarization competes for the available current at the surface of the electrode. As soon as current becomes lower in some region, electrode passivity will be reestablished [12, 14]. In view of this, there is a gradual reduction in current associated to HER as part of the regions stops propagating.

2.3.4. Tafel polarization analysis of Fe electrodes

The Tafel polarization curves of the commercialized Fe with and without MoS₂ additives are displayed in Figure 2.6 while Table 2.4 shows the corrosion potentials (E_{corr}) and the corrosion currents (I_{corr}) gotten from the linear equation fittings of current density as a function of potential, while the inhibition efficiency (IE) was estimated via the formula in equation 2.5 below [36, 37]:

$$E. I \% = (j_{corr}^0 - j_{corr}) / (j_{corr}^0 \times 100) \quad [2.5]$$

Interestingly, as potential shift to a more positive region, the bare Fe electrode exhibits a transient behavior from anodic to cathodic reaction around a potential of -0.93 V to -0.96 V and a current of 1.5 A to 1.3 A. Thus, the electrode is said to exhibit both HER and passivation effect at this point. It is worthy to note that as polarization was interrupted due to HER, there was a progressive drop in potential which was later accompanied by a sudden rise in current prior to the occurrence of trans-passive dissolution. In the case of F10M, a sudden rise in current from -1.9 A to -1.6 A determined by potentiostat was related to passivation. As potential shift to the more positive region, more passivation occurred as the current determined by potentiostat increases progressively. However, current drop associated to HER was observed around -1.6 A and -1.8 A. From Table 2.4, both F10M battery and the bare Fe electrode show higher corrosion currents, which may be ascribed to their crystalline

structures. According to XRD, both samples have two highest peaks intensity at (020) and (200) facets. Hence, the corrosion current at these two planes may be high. The F3M and F5M also display high peaks intensity at (110) and (002) with low reactive (200) plane on the surface, which may be responsible for the low corrosion rate in F3M and F5M. Thus, the corrosion rate decreased in the order bare Fe > F10M > F5M > F3M. This result is not surprising to us because of the increased surface area revealed in the SEM images (Figure 2.2), because the rate of corrosion perceived on a material surface is relative to its surface area.

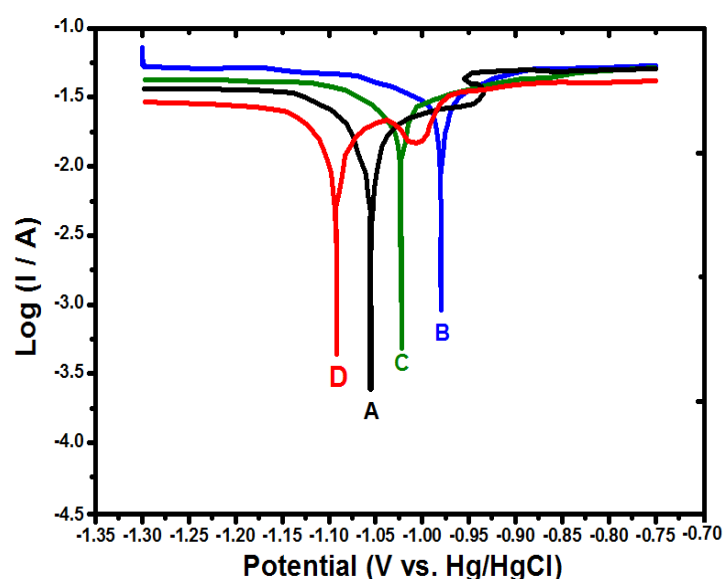


Figure 2.6. Tafel plots of (a) bare Fe, (b) F3M, (c) F5M, and (d) F10M.

Table 2.4. Electrochemical kinetics parameters of Tafel curves.

Sample	j_{corr} (mA cm^{-2})	E_{corr} (V vs. Hg/HgCl)	E.I %
Bare Fe	2.0128×10^{-2}	-1.0543	-
F3M	0.9826×10^{-2}	-0.9796	51.2
F5M	1.5877×10^{-2}	-1.0219	21.1
F10M	1.8941×10^{-2}	-1.0906	5.6

2.3.5. Linear polarization resistance analysis of Fe electrodes

Figure 2.7(a-b) depicts the current change during cathodic deposition of the various samples for 5500 seconds at 1.0 V in 6 M KOH solution with and without 2 mM Na₂S electrolyte additive. In Figure 2.7(a), a dramatic rise in current due to passivation was formed on the surface of the bare Fe electrode compare to Figure 2.7(b) where almost 50 % current drop was observed. Upon the addition of MoS₂ composites to the electrode (ie. F3M, F5M, and F10M), the current-time response was more flattened. Among them, a constant current was best maintain in the F3M and F5M anodes in the 6M KOH solution containing 2mM Na₂S electrolyte additive as shown in Figure 2.7b. In the case of F10M electrode, the response was more linear in the presence of Na₂S than in 6 M KOH electrolyte solution. Thus, Fe-MoS₂ composite has a more positive electrode potential than bare Fe. We affirmed this by increasing the MoS₂ in the electrode (F5M and F10M) which gave rise to rise in current.

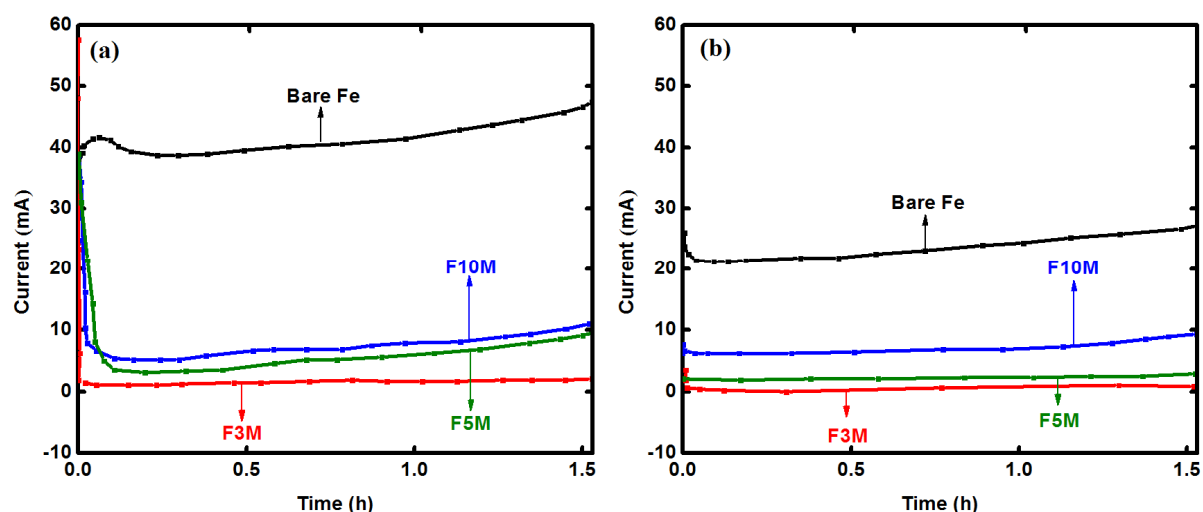


Figure 2.7. Current as a function of time of various anodes in (a) 6 M KOH, and (b) 6 M KOH solution with Na₂S electrolyte additive.

2.3.6. Capacity Retention / Efficiency study of Fe electrodes

Figure 2.8 shows the performances after assembling the full cell batteries. At the 800th cycle, the capacities of the batteries were 290 mAh/g-F3M, 280 mAh/g-F5M, and 230 mAh/g-F10M respectively. Except for the bare Fe battery, all the assembled cells show drastically enhanced cyclability up to 800th cycles. From the Fe batteries with F3M, F5M, and F10M, the mean capacity retention (%) gotten after 800th cycles were 97 %, 92 %, and 77 % respectively. This excellent performance affirms to the unique structure of MoS₂ additives on the Fe surface. After 300th cycles, we saw a drastic capacity drop below 65% in the case of the bare Fe batteries arising as a result of hydrogen gas effect, high dissolution of Fe, and shape change at the Fe anode. At this junction, dramatic fluctuation occurs in the coulombic efficiency.

The recovery of this drastic capacity drop happened in just 6 cycles upon addition of 3wt.% MoS₂ additive to the bare Fe electrode (ie. F3M). These results confirm the role of sulfide towards maintaining long life cycle of Fe secondary batteries. About 23% of the original capacity was loss during battery failure in the case of F10M. This loss was due to the large surface area of the F10M battery which leads to the generation of hydrogen gas bubbles (HER) at the surface of the electrode. Likewise, the XRD peaks at (020) and (200) planes are high. According to Sun *et al.*, HER is most likely to take place at this crystal surface while the (110) peak is less affected by HER effect [25]. While this effect increases, the F10M anode surface increase and as a result, the failure of the battery rapidly occurs. This account for the enhanced battery performance of F3M and F5M due to low corrosion and passivation effects. Apart from the F10M, all the battery samples can reduce the side effect of Fe metal-air batteries among which, the F3M batteries show superior performance.

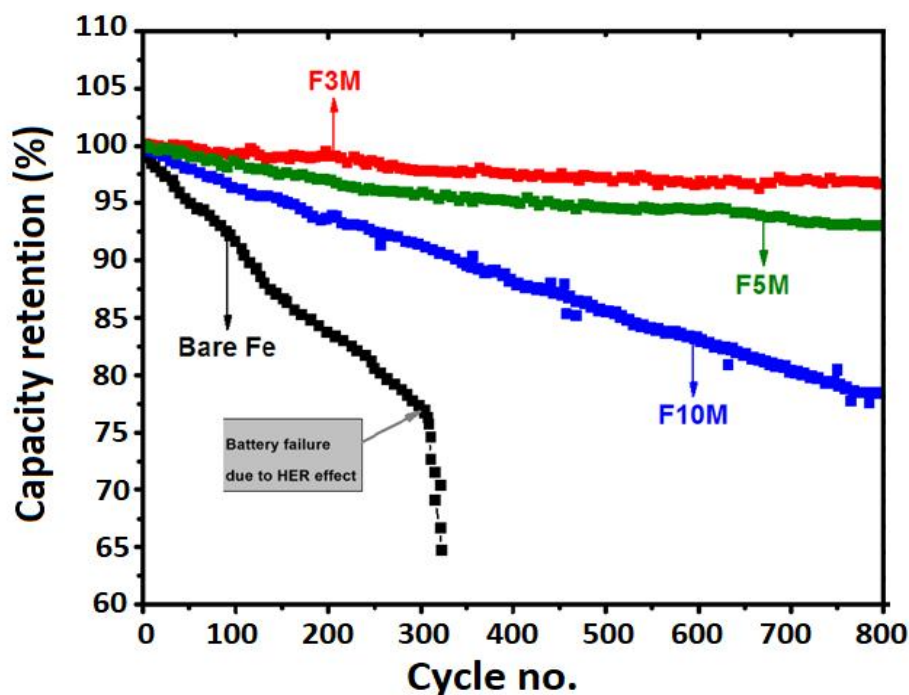


Figure 2.8. Batteries cyclability of various electrodes in 6 M KOH + 2 mM Na₂S electrolyte.

To maintain full capacity, the batteries were charged at a constant current for 7 consecutive days until the float voltage 1.0 V was attained. This approach has been extensively adopted in literature to assess batteries performance at 100 % state-of-charge (SOC) [38-40]. The set current is known as the “float charge current (FCC)” needed to assess the current that is meant to maintain the cells at 100 % SOC. Lower current implies that less energy is needed for the purpose. Figure 2.9 shows the plot of FCC of the batteries using the bare Fe, F3M, F5M, and F10M, respectively. Among the various anodes, F3M displayed the lowest float currents while the bare Fe anode displayed the highest float currents. This result suggests that the batteries side reactions (such as HER) are mitigated successfully within the F3M cell compare to others. The F5M battery anode displays the next lowest float current after the F3M battery anode. Because of the higher surface area of F10M battery anode, we observed that the float current was higher than the F5M battery anode but lower than the bare Fe anode. Hence, the surface refinement of Fe with F10M is not as functional as with F3M and F5M electrodes.

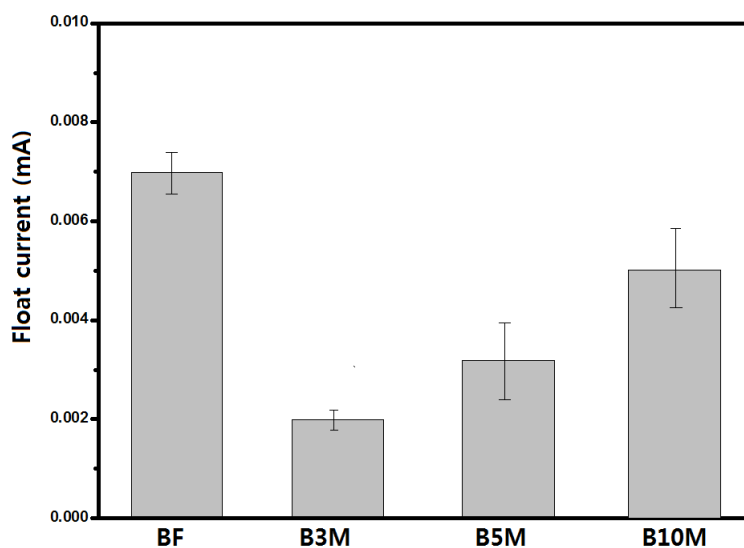


Figure 2.9. Float current of Fe batteries with different composition of MoS₂ additives.

2.3.7. Energy dispersive X-ray spectroscopy of F3M battery

We carried out FE-EDS analysis to verify the quantity of MoS₂ present in the anode. Figure 2.10(a-b) elucidated on the relative abundance of the individual chemical element present in the various electrodes. EDS analysis detected the presence of C, Fe, Mo, S, and O in the electrode. In accordance to images, the exact quantities of MoS₂ deposited in the F3M, F5M, and F10M electrodes were 3.02 wt.%, 5.0 wt.%, and 10.01 wt.% respectively, as shown in Table 2.5. We also observed that one of the peaks below 2 keV corresponds to oxygen present in the electrodes. The exact quantity of oxygen present was found to be 2.01 wt.%, 1.06 wt.%, 1.01 wt.% and 0.98 wt.% in the bare Fe, F3M, F5M, and F10M electrodes respectively. Apart from this, EDS could not trace the presence of any other elements.

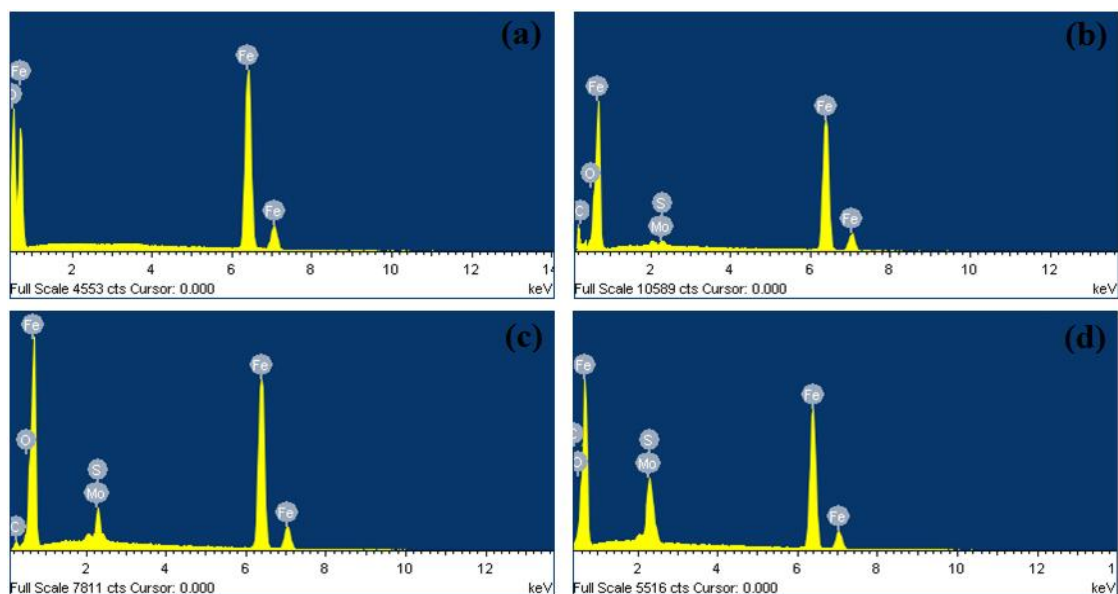


Figure 2.10. EDS images of (a) bare Fe, (b) F3M, (c) F5M, and (d) F10M composites after cycling.

Table 2.5. Relative abundance of individual chemical element content present in the electrodes.

Samples	Bare Fe		F3M		F5M		F10M	
	wt. %	at. %	wt. %	at. %	wt. %	at. %	wt. %	at.%
Fe	89.56	65.96	87.91	66.29	85.67	63.86	80.54	59.17
C	8.43	28.87	8.01	28.09	8.32	28.84	8.47	28.93
Mo	-	-	1.30	0.57	2.11	0.92	4.01	1.71
S	-	-	1.72	2.26	2.89	3.75	6.00	7.68
O	2.01	5.17	1.06	2.79	1.01	2.63	0.98	2.51
Total	100	100	100	100	100	100	100	100

2.4. Conclusions

A cost effective and facile strategy was used to investigate the performance and behavior of high purity carbonyl Fe-MoS₂ composites (bare Fe, F3M, F5M, and F10M). In conjunction with the unique structure and synergistic effect that characterizes two excellent anode materials, the carbonyl Fe-MoS₂ shows excellent electrochemical properties. X-ray diffraction (XRD) and field emission scanning electron microscopy (FE-SEM) reveals that the various additives produce distinct morphological surface structure that corresponds to the fundamental crystallographic growth patterns. SEM mapping shows a well distributed MoS₂ and Fe in the composite mixture. Additionally, energy dispersive spectroscopy (EDS) affirms the relative abundance of the individual elements deposited in the electrode. During CV analysis, F3M shows superior redox peak associated to the stable pathway of our choice of electrolyte additive within the electrode. It is worth noting that MoS₂ functioned as both anodically and cathodically active material. As a result, HER and passivation effect occurring during cathodic and anodic polarization were mitigated successfully in the bare Fe. According to Tafel test, the corrosion rate decreased in the order of bare Fe > F10M > F5M > F3M. Thus, this finding affirms to us that an excess amount of MoS₂ beyond 3wt. % is not advisable for an excellent rechargeable Fe-air battery. With all this indices and yardstick, high purity F3M composite electrode via 6M KOH (with Na₂S additive) solution may pave a pathway for the development of a cost-effective anode electrode material for Fe-air batteries.

2.5. References

1. B. Tian, J. Światowska, V. Maurice, S. Zanna, A. Seyeux, P. Marcus, The effect of Na₂S additive in alkaline electrolyte on improved performances of Fe-based air batteries, *Electrochimica Acta* 259 (2018) 196–203.
1. J.O.G. Posada, P. Hall, Controlling hydrogen evolution on iron electrodes, *International Journal of Hydrogen Energy* 41(2016) 20807–20817.
2. X. Yu, A. Manthiram, A Voltage-Enhanced, Low-Cost Aqueous Iron–Air Battery Enabled with a Mediator-Ion Solid Electrolyte, *ACS Energy Letter* 2 (2017) 1050–1055.
3. B. Yang, S. Malkhandi, A.K. Manohar, G.K.S. Prakash, S.R. Narayanan, Organo-sulfur molecules enable iron-based battery electrodes to meet the challenges of large-scale electrical energy storage, *Energy Environment Science* 7 (2014) 2753–2763.
4. *Grid Energy Storage*, US Department of Energy, December 2013 available at <http://energy.gov/oe/downloads/grid-energy-storage-december-2013>.
5. A.K. Manohar, C. Yang, S. R. Narayanan, The Role of Sulfide Additives in Achieving Long Cycle Life Rechargeable Iron Electrodes in Alkaline Batteries, *Journal of the Electrochemical Society* 162 (2015) A1864–A1872.
6. T. Kim, Y. Ohata, J. Kim, C.K. Rhee, J. Miyawaki, S. Yoon, *Carbon* 80 (2014) 698–705.
7. H. Wang, Y. Liang, M. Gong, Y. Li, W. Chang, T. Mefford, J. Zhou, J. Wang, T. Regier, F. Wei, H. Dai, *Journal of Material Chemistry-A* 5 (2017) 1558–1566.
8. Y. Yang, F. Scenini, M. Curioni, A study on magnesium corrosion by real-time imaging and electrochemical methods: Relationship between local processes and hydrogen evolution, *Electrochimica Acta* 198 (2016) 174–184.
9. G.S. Frankel, S. Fajardo, B.M. Lynch, Introductory lecture on corrosion chemistry: a focus on anodic hydrogen evolution on Al and Mg. *Faraday Discuss* 180 (2015) 111–133.
10. R. Liu, S. Thomas, J. Scully, G. Williams, N. Birbilis, An experimental survey of the

cathodic activation of metals including Mg, Sc, Gd, La, Al, Sn, Pb and Ge in dilute chloride solutions of varying pH, *Corrosion Science* 73 (2017) 494–505.

11. M. Pourbaix, Application of electrochemistry in corrosion science and in practice, *Corrosion Science* 14 (1974) 25–82.
12. R.D. McKerracher, C.P. Leon, R.G.A. Wills, A.A. Shah, F.C. Walsh, A Review of the Iron–Air Secondary Battery for Energy Storage, *ChemPlusChem* 80 (2014) 1–14.
13. X. Han, X. Li, J. White, C. Zhong, Y. Deng, W. Hu, T. Ma, Metal–Air Batteries: From Static to Flow System, 2018, <http://doi.org/10.1002/aenm.201801396>.
14. X. Han, G. He, Y. He, J. Zhang, X. Zheng, L. Li, C. Zhong, W. Hu, Y. Deng, T.Y. Ma, Engineering Catalytic Active Sites on Cobalt Oxide Surface for Enhanced Oxygen Electrocatalysis, *Advanced Energy Materials* 3 (2018) 13394–13397.
15. X. Han, X. Wu, Y. Deng, J. Liu, J. Lu, C. Zhong, W. Hu, Ultrafine Pt Nanoparticle-Decorated Pyrite-Type CoS₂ Nanosheet Arrays Coated on Carbon Cloth as a Bifunctional Electrode for Overall Water Splitting, *Advanced Energy Materials* 80 (2018) 935–943.
16. C. Laurent, F. Scenini, T. Monetta, F. Bellucci and M. Curioni, The contribution of hydrogen evolution process during corrosion of aluminum and aluminum alloys investigated by potentiodynamic polarization coupled with real time hydrogen measurement, *Material Degradation* 6 (2017) 41529–41532.
17. W.A Mueller, Theory of the polarization curve technique for studying corrosion and electrochemical protection, *Canada Journal of Chemistry* 38 (1960) 576–587.
18. Y. Zhang, Y. Wang, J. Yang, W. Shi, H. Yang, W. Huang, X. Dong, MoS₂ coated hollow carbon spheres for anodes of lithium ion batteries, *2D Materials* 3 (2016) 024001–024012.
19. L. Leng, S. Liao, Enhanced Performance of Li-O₂ Batteries with MoS₂ Nanosheet-Coated TiN Nanorods Arrays Grown on Carbon Paper as Binder-Free Cathodes, *Abstract 116* (2016) 1–3.
20. P. Tan, H.R. Jiang, X.B. Zhu, L. An, C.Y. Jung, M.C. Wu, L. Shi, W. Shy, T.S. Zhao, Advances and challenges in lithium-air batteries, *Applied Energy* 204 (2017) 780–806.

21. H. Li, K. Yu, C. Li, Z. Tang, B. Guo, X. Lei, H. Fu, Z. Zhu, Charge transfer induced high efficient hydrogen evolution of MoS₂/graphene Co-catalyst, *scientific Report* 5 (2015) 18730–18753.
22. J. Hu, C. Zhang, L. Jiang, H. Lin, Y. An, D. Zhou, M.K.H. Leung, S. Yang, Nanohybridization of MoS₂ with layered double hydroxides efficiently synergizes the hydrogen evolution in alkaline media, *Joule* 1 (2017) 383–393.
23. B. Qu, Y. Sun, L. Liu, C. Li, C. Yu, X. Zhang, Y. Chen, Ultrasmall Fe₂O₃ nanoparticles/MoS₂ nanosheets composite as high-performance anode material for lithium ion batteries, *Scientific Reports* 7 (2017) 42772–42776.
24. P. Sun, W. Zhang, X. Hu, L. Yuan, Y. Huang, Synthesis of hierarchical MoS₂ and its electrochemical performance as an anode material for lithium-ion batteries, *Journal of Material Chemistry A* 2 (2014) 3498–3505.
25. Y. Teng, H. Zhao, Z. Zhang, Z. Li, Q. Xia, Y. Zhang, L. Zhao, X. Du, Z. Du, P. Lv, K. Świerczek, MoS₂ Nanosheets Vertically Grown on Graphene Sheets for Lithium-Ion Battery Anodes, *ACS Nano* 10 (2016) 8526–8535.
26. A.K. Manohar, C. Yang, S. Malkhandi, G.K.S. Prakash, S.R. Narayanan, Enhancing the performance of the rechargeable iron electrode in alkaline batteries with bismuth oxide and iron sulfide additives, *Journal Electrochemistry Society* 160 (2013) 78–84.
27. A.S. Rajan, M.K. Ravikumar, K.R. Priolkar, S.Sampath, A.K. Shukla, Carbonyl-Iron electrodes for rechargeable-iron batteries, *Electrochemistry Energy Technology* 1 (2014) 2–9.
28. D.J. Park, E.O. Aremu, K.S. Ryu, Bismuth oxide as an excellent anode additive for inhibiting dendrite formation in zinc-air secondary batteries, *Applied Surface Science* 456 (2018) 507–514.
29. X. Han, X. Ling, Y. Wang, T. Ma, C. Zhong, W. Hu, Y. Deng, Generation of nanoparticle, atomic-cluster, and single-atom cobalt catalysts from zeolitic imidazole frameworks by spatial isolation and their use in zinc-air batteries, *Angewandte chemie*, 35 (2019) 109–112.

30. K.O. Nayana, T.V. Bright, Zinc electrodeposition and study of influence of synergistic interaction of additives on coating properties, *Journal of industrial engineering chemistry* 26 (2015) 107–115.
31. X. Han, W. Zhang, X. Ma, C. Zhong, N. Zhao, W. Hu, Y. Deng, Identifying the activation of bimetallic sites in NiCo₂S₄@g-C₃N₄-CNT hybrid electrocatalysts for synergistic oxygen reduction and evolution, *advanced materials*, 8 (2018) 281–287.
32. B.T. Hang, T. Watanabe, M. Egashira, I. Watanabe, S. Okada, J. Yamaki, The effect of additives on the electrochemical properties of Fe/C composite for Fe/air battery anode, *Journal of Power Source* 155 (2006) 461–469.
33. H. Weinrich, J. Come, H. Tempel, H. Kungl, R.A. Eichel, N. Balke, Understanding the nanoscale redox-behavior of iron-anodes for rechargeable iron-air batteries, *Nano Energy* 41 (2017) 706–716.
34. E.O. Aremu, D.J. Park, K.S. Ryu, The effect of anode additives towards suppressing dendrite growth and hydrogen gas evolution in Zn-air secondary batteries, *Ionics*, 25 (2019) 4197–4207.
35. W. Tingting, Y. Zhanhong, Y. Bin, W. Ruijuan, H. Jianhang, The electrochemical performances of Zn-Sn-Alhydrotalcites in Zn-Ni secondary cells, *Journal of Power Source* 257 (2014) 174–180.
36. O. Seri, B. Siree, The differentiating polarization curve technique for the tafel parameter estimation, *Catalysts* 7 (2017) 239.
37. J.J. Niu, B.E. Conway, W.G. Pell, Comparative studies of self-discharge by potential decay and float-current measurements at C double-layer capacitor and battery electrodes, *Journal of Power Sources* 135 (2004) 332–343.
38. R. Dufo-Lopez, J.M. Lujano-Rojas, J.L. Bernal-Agustín, Comparison of different lead-acid battery lifetime prediction models for use in simulation of stand-alone photovoltaic systems. *Applied Energy* 115 (2014) 242–253.
39. H.B. Zhao, C.J. Hu, H.W. Cheng, J.H. Fang, Y.P. Xie, W.Y. Fang, T.N.L. Doan, T.K.A. Hoang, J.Q. Xu, P. Chen, Novel rechargeable M₃V₂(PO₄)₃//Zinc (M = Li, Na) hybrid

aqueous batteries with excellent cycling performance, *Science Report* 6 (2016) 25809–25819.

40. A. Wassilkowska, A. Czaplicka-Kotas, M. Zielina, A. Bielski, An analysis of the elemental composition of micro-samples using EDS technique, *Chemical Transaction Chemistry* 18 (2014) 133–148.

Recent Awards and Honors

- 2018 Lifetime membership award, Lions club international.
- 2019 Managing safely, Institution of occupational safety and health, United Kingdom
(Under the umbrella wing of HSEi, India).

List of Publications

1. Park, D.J., Aremu, E.O., Ryu, K.S., Bismuth oxide as an excellent anode additive for inhibiting dendrite formation in zinc-air secondary batteries, *Applied Surface Science*, 456 (2018) 507–514.
2. Aremu, E.O., Park, D.J. & Ryu, K.S, The effect of anode additives towards suppressing dendrite growth and hydrogen gas evolution in Zn-air secondary batteries, *Ionics* 25 (2019), 4197–4207.
3. Aremu, E.O., Ryu, K.S., Performance and Degradation Behavior of Carbonyl Fe – MoS₂ Composite as Anode Material in Fe-air Batteries, *Electrochimica Acta*, 313, (2019), 486– 477.
4. Aremu, E.O., Ryu, K.S., The inhibitory effects of CuO additives on hydrogen evolution reaction in Fe anode materials for Fe-air batteries – **(Manuscript under review on “International Journal of Hydrogen Energy”)**.

Conferences and Seminars Presentation

1. **Emmanuel Olugbemisola Aremu** and Kwang-Sun Ryu, An investigation of the Electrochemical properties of molybdenum (IV) sulfide as anode additive for secondary iron air Batteries, 19th International Meeting on Lithium Batteries (IMLB), KICC, Japan (2018).
2. **Emmanuel Olugbemisola Aremu** and Kwang-Sun Ryu, Performance and Degradation Behavior of Carbonyl Fe – MoS₂ Composite as Anode Material in Fe-air Batteries, Korea Electrochemical Society conference, Korea (2019).
3. **Emmanuel Olugbemisola Aremu** and Kwang-Sun Ryu, The effect of CuO and LiOH additives in (Fe)_x + (MoS₂)_y composites as anode materials for rechargeable Fe-air batteries, Korean Battery Society Conference, Korea (2019).